



HAL
open science

Insights Into Venus' Crustal Plateaus From Dyke Trajectories Below Craters

Alexandra Le Contellec, Chloé Michaut, Francesco Maccaferri, Virginie Pinel, Frédéric Chambat, Suzanne Smrekar

► **To cite this version:**

Alexandra Le Contellec, Chloé Michaut, Francesco Maccaferri, Virginie Pinel, Frédéric Chambat, et al.. Insights Into Venus' Crustal Plateaus From Dyke Trajectories Below Craters. *Journal of Geophysical Research. Planets*, 2024, 129 (5), pp.e2023JE008189. 10.1029/2023JE008189 . hal-04564433

HAL Id: hal-04564433

<https://hal.science/hal-04564433>

Submitted on 30 Apr 2024

HAL is a multi-disciplinary open access archive for the deposit and dissemination of scientific research documents, whether they are published or not. The documents may come from teaching and research institutions in France or abroad, or from public or private research centers.

L'archive ouverte pluridisciplinaire **HAL**, est destinée au dépôt et à la diffusion de documents scientifiques de niveau recherche, publiés ou non, émanant des établissements d'enseignement et de recherche français ou étrangers, des laboratoires publics ou privés.

Insights Into Venus' Crustal Plateaus From Dyke Trajectories Below Craters



Key Points:

- We identify four different behaviors for magma-filled crack propagation below craters
- We draw a behavior diagram as a function of two dimensionless numbers characterizing dyke propagation below a crater
- Magma infilling of dark-floored craters in Venus' plateaus requires a crustal thickness ≤ 45 km and a small crust-magma density contrast

Supporting Information:

Supporting Information may be found in the online version of this article.

Correspondence to:

A. Le Contellec,
alexandra.le_contellec@ens-lyon.fr

Citation:

Le Contellec, A., Michaut, C., Maccaferri, F., Pinel, V., Chambat, F., & Smrekar, S. (2024). Insights into Venus' crustal plateaus from dyke trajectories below craters. *Journal of Geophysical Research: Planets*, 129, e2023JE008189. <https://doi.org/10.1029/2023JE008189>

Received 2 NOV 2023
Accepted 9 APR 2024

Author Contributions:

Conceptualization: Alexandra Le Contellec, Chloé Michaut, Virginie Pinel
Data curation: Alexandra Le Contellec
Formal analysis: Alexandra Le Contellec, Chloé Michaut, Francesco Maccaferri, Virginie Pinel, Frédéric Chambat
Funding acquisition: Chloé Michaut
Investigation: Alexandra Le Contellec, Chloé Michaut, Francesco Maccaferri
Methodology: Alexandra Le Contellec, Chloé Michaut, Francesco Maccaferri, Virginie Pinel
Project administration: Chloé Michaut
Software: Alexandra Le Contellec, Francesco Maccaferri
Supervision: Chloé Michaut, Virginie Pinel

© 2024 The Authors.

This is an open access article under the terms of the [Creative Commons Attribution-NonCommercial License](https://creativecommons.org/licenses/by-nc/4.0/), which permits use, distribution and reproduction in any medium, provided the original work is properly cited and is not used for commercial purposes.

Alexandra Le Contellec¹ , Chloé Michaut^{1,2} , Francesco Maccaferri³ , Virginie Pinel⁴ , Frédéric Chambat¹, and Suzanne Smrekar⁵

¹Laboratoire de Géologie de Lyon: Terre, Planète, Environnement, Ecole Normale Supérieure de Lyon, Université de Lyon, Université Claude Bernard Lyon 1, Lyon, France, ²Institut Universitaire de France, Paris, France, ³INGV, Instituto Nazionale di Geofisica e Vulcanologia, Sezione di Napoli - Osservatorio Vesuviano, Napoli, Italy, ⁴Université Grenoble Alpes, Université Savoie Mont Blanc, CNRS, IRD, Université Gustave Eiffel, ISTERre, Grenoble, France, ⁵Jet Propulsion Laboratory, California Institute of Technology, Pasadena, CA, USA

Abstract On Venus, radar observations of the surface have highlighted two categories of craters: bright-floored, interpreted as pristine, and dark-floored, interpreted as being partially filled by lava. While volcanic resurfacing occurs within and outside craters in the plains, it seems mainly concentrated within the interior of dark-floored craters in the crustal plateaus, suggesting that the magma is negatively buoyant there. Indeed, crater unloading may facilitate vertical ascent of a negatively buoyant magma by decompressing the underlying crust. However, the crater topography also generates a shear stress which would tend to horizontalize the vertical propagation of a dyke. We use numerical simulations of magma ascent in an axisymmetric crater stress field to demonstrate that, depending on the crust thickness and the magma-crust density contrast, a negatively buoyant magma can indeed erupt only in the crater interior while remaining stored in the crust elsewhere. In particular, we identify four different behaviors depending on if and where a magma-filled crack ascending below a crater reaches the surface. We draw a regime diagram as a function of two characteristic dimensionless numbers. For eruption to occur only in the crater interior requires a crust thinner than 45 km and a limited range of magma-crust density contrasts, between 40 and 280 kg m⁻³ for crust thicknesses between 20 and 45 km, the permissible range decreasing for increasing crustal thicknesses. These results suggest that the crustal plateaus may not be particularly thick and could be slightly differentiated, but probably not very felsic.

Plain Language Summary The Magellan mission revealed two categories of impact craters at the surface of Venus: the pristine bright-floored and the dark-floored craters, which are interpreted as craters partially filled by smooth lava after their formation. In the crustal plateaus of Venus, the magma reaches the surface mainly within craters, suggesting that it is denser than the crust. Because of the crater negative topography, the underlying crust is decompressed relative to its surroundings, which, in turn, facilitates magma ascent below the crater despite its negative buoyancy. We first gather surface observations on a set of craters located in the crustal plateaus of Venus to construct a characteristic fresh crater topography. We then use a model of magma ascent below a crater in the crust of Venus to constrain the magma and crust densities as well as the initial magma storage depth that allow for magma eruption within the crater interior only. We show that magma reaches the surface only in the interior of the crater if the crust is slightly less dense than the magma and if it is not too thick (≤ 45 km in thickness).

1. Introduction

Observations of the surface of Venus by the Venera, Magellan, and Venus Express missions revealed vast volcanic plains at low topographies making up most of the planet surface. Only about a thousand impact craters are visible, having a global random distribution (Phillips et al., 1992), which suggests a relatively recent resurfacing of the planet. Whether this resurfacing was a catastrophic event or is a progressive and ongoing process is still a matter of debate (Herrick & Phillips, 1994; Romeo & Turcotte, 2010; Strom et al., 1994). On average, the number and size of craters point to a relatively young surface of 250–750 million years old (Hauck et al., 1998; Herrick & Rumpf, 2011; Phillips et al., 1992; Schaber et al., 1992; Strom et al., 1994).

Contrasting with these low lava plains, the crustal plateaus culminate 2–4 km above the mean planetary radius (Phillips & Hansen, 1994), but encompass less than 8% of the surface of Venus (M. Ivanov & Head, 1996, 2011). These plateaus are not to be mistaken with the volcanic rises, such as Western Eistla, Beta

Validation: Alexandra Le Contellec, Chloé Michaut, Virginie Pinel
Visualization: Alexandra Le Contellec
Writing – original draft: Alexandra Le Contellec, Chloé Michaut
Writing – review & editing: Francesco Maccaferri, Virginie Pinel, Frédéric Chambat, Suzanne Smrekar

and Atla Regios, which are believed to originate from volcanic hotspots (Stofan & Smrekar, 2005). The topography of the crustal plateaus is strongly correlated with negative Bouguer anomalies, suggesting that they could be isostatically compensated (James et al., 2013; Jiménez-Díaz et al., 2015; S. E. Smrekar & Phillips, 1991) and that their high topography is associated with crustal thickening. However the process at the origin of this thickening is still unknown.

Crustal plateaus are dominated by tile-like tessera terrains (Barsukov et al., 1986; Basilevsky et al., 1986). Tesserae were first characterized from Venera 15 and 16 observations; they present numerous ridges, grabens and faults resulting from multiple episodes of deformation (M. Ivanov & Head, 1996) both in contraction and extension. Tesserae are mainly found as large expanses, in particular in Ovda and Thetis Regios or Fortuna Tessera, but they can also be found as small inliers or even patches in the plains. Their low surface coverage and their small number of craters make it difficult to infer a statistically significant age for these plateaus. Yet, they are thought to represent the oldest crustal structures on Venus based on stratigraphic studies (Basilevsky & Head, 1998; M. Ivanov & Head, 1996). The origin of these old, multiply deformed terrains is widely debated. While some authors proposed they originate from a mantle plume (Hansen et al., 2000; Phillips et al., 1991), others suggest they could have formed from mantle downwelling due to mantle coldspots (Bindschadler et al., 1992; Gilmore & Head, 2000), or from large lava ponds caused by mantle melting resulting from large bolide impacts on an ancient thin lithosphere (Hansen, 2006). Lately, Romeo and Turcotte (2010) and Romeo and Capote (2011) suggested that these tesserae could be the remnant of a differentiated crust similar to the continental crust on Earth.

The knowledge of the nature of the crust forming these plateaus would bring strong constraints on the geodynamic process from which they originate. It is however still quite enigmatic. Seven landers of the Venera and Vega programs have performed analyses to constrain the crustal composition of Venus. Most of the landers settled in the plains of the planet (in Navka Planitia for Venera 8, 13, and 14, and in Rusalka Planitia for Vega 1), with the exception of Venera 9, 10, and Vega 2, which landed on volcanic rises (Venera 9 and 10 landed on the flank of eastern Beta Regio and Vega 2 on a lava flow on Atla Regio) (Kargel et al., 1993). No tessera plateau terrains *per se* were sampled and analyzed during these missions. K-U-Th content measurements by γ -ray and X-ray fluorescence were performed at the landing sites of Venera 8, 9, 10, 13, and 14 and Vega 1 and 2. In addition, Venera 13, 14, and Vega 2 performed major element content analyses and took panoramic pictures of the surrounding terrain (Surkov et al., 1983, 1984, 1986). Major element analyses at the landing sites of Venera 13, 14, and Vega 2 suggests a basaltic composition similar to alkaline and tholeiitic series on Earth (Basilevsky et al., 2007) for the plains and the volcanic rises. Measured radiogenic element concentrations were similar to that of tholeiitic basalts except at the Venera 8 and 13 landing sites, where these concentrations were particularly high, suggesting more differentiated alkaline lavas (Basilevsky et al., 2007). Overall, measurements are consistent with a mafic composition.

Information on the surface composition were also gathered from orbit by Visible and Infrared Thermal Imaging Spectrometer (VIRTIS) (Helbert et al., 2008; Mueller et al., 2008) onboard Venus Express as well as Near Infrared Mass Spectrometer (NIMS) onboard Magellan (Hashimoto et al., 2008). Thermal emissivity data obtained by both instruments show a lower surface emissivity in the tessera plateaus than in the plains at $\sim 1 \mu\text{m}$ (Gilmore et al., 2015, 2017; Hashimoto et al., 2008; Helbert et al., 2008; Mueller et al., 2008), suggesting that there may be compositional differences between the two types of terrains. Emissivity values suggest a felsic composition in the tessera plateaus, potentially similar to granitic rocks on Earth (Gilmore et al., 2015; Hashimoto et al., 2008), while the high surface emissivity measured in the plains and on volcanic rises (Mueller et al., 2008) are in agreement with a basaltic composition. The Synthetic Aperture Radar (SAR) instrument of Magellan also gave information on surface roughness. The plateaus appear much brighter in reflected radar data than the plains, indicating a smoother material in the plains than in the tectonically deformed plateaus (Basilevsky & Head, 2003; M. Ivanov & Head, 2011). Combined altogether, these different types of observations -radiogenic and major elements analysis, surface emissivity in the atmospheric window- tend to indicate that the material making up the plains is basaltic, whereas the tessera plateaus could be more felsic.

Radar observations from the Venera 15/16 and Magellan missions show two main categories of craters on Venus: radar bright-floored and dark-floored craters (B. Ivanov, 1990; Herrick & Phillips, 1994). The Magellan mission allowed for a full inventory of impact craters. Its radar observed Venus with an inclination angle of 17° – 47° ; over most of this angle, radar backscatter (or image brightness) is predominantly a function of surface roughness at the

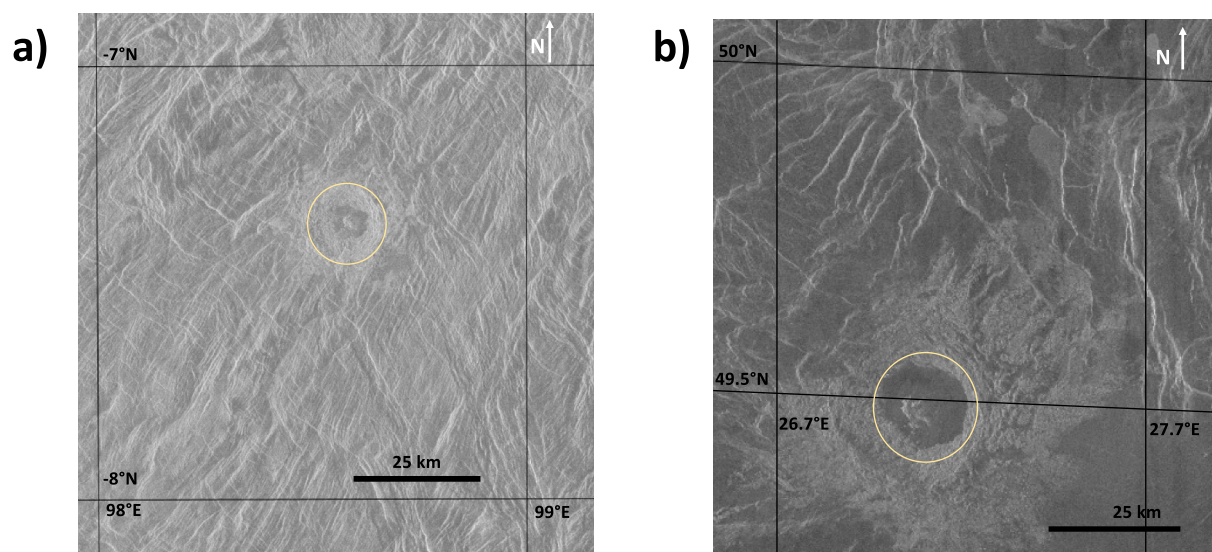


Figure 1. Examples of dark-floored craters and their highly deformed surroundings: (a) Chloe and (b) Kauffman (see topographic profiles in Figure 2).

radar wavelength, which is ~ 12 cm for Magellan radar. Bright portions of an image indicate significant surface roughness that causes the radar wave to scatter, allowing much of the radar wave to reflect back to the spacecraft. A radar dark surface is smooth at the 12 cm scale due to the radar wave reflecting away from the spacecraft. Grieve and Cintala (1995) suggested that the floor brightness is a function of impact melt volumes, with large melt volumes creating smooth crater floors as well as the runout flows seen exterior to a small number of craters. However Wichman (1999) found that dark-floored craters generally have similar to slightly larger radii than the bright floored craters. The predominant interpretation also includes analysis of the extended ejecta deposits to conclude that bright-floored craters represented young and fresh craters (especially if exhibiting unaltered dark parabolas) (Campbell et al., 1992), while dark-floored craters have undergone surface modification subsequent to crater formation. Izenberg et al. (1994) suggested that surface weathering and aeolian deposits on crater floors could explain the radar dark, smooth surfaces. However, Sharpton (1994) and Herrick and Phillips (1994) noticed that dark-floored craters have shallower floors than the bright-floored ones in Magellan altimetry data, an observation which was later confirmed using higher resolution stereo topography data (Herrick & Rumpf, 2011; Herrick et al., 2012). Of all possible processes, including aeolian deposits, impact melting or surface weathering, volcanic resurfacing of the crater floor seems the most plausible to explain the depth-to-radius relationship shown by dark-floored craters (Wichman, 1999).

Volcanic resurfacing depends not only on the presence of mantle melt but also on the crust properties and magma buoyancy. It is facilitated if the crust is mafic and thin, as it may be in the plains, and less so if the crust is thicker and more felsic. The crustal plateaus are supposedly the oldest structures of Venus (Basilevsky et al., 1987; M. Ivanov & Basilevsky, 1993); they have preserved the imprint of their tectonic history. In the plains, regional volcanism leads to volcanic resurfacing both inside and outside craters (Herrick & Rumpf, 2011). On the contrary, in the plateaus, limited evidence of abundant resurfacing is visible, mainly in the form of dark-floored craters (Herrick & Phillips, 1994; Herrick & Rumpf, 2011; Phillips et al., 1992; Sharpton, 1994). Volcanic flooding in these craters seems to originate from the crater interior, as the ejecta blankets resulting from the impact process show no evidence of crosscutting and appear complete in SAR images (Figures 1 and 2). This suggests that the magma is denser than the crust in the plateaus and that magma ascent and eruption is facilitated by crater unloading there. On the Moon, the highly porous, anorthite-rich crust strongly inhibits magma ascent (Head & Wilson, 1998). But Michaut and Pinel (2018) and Michaut et al. (2020) have shown that crater-induced unloading could facilitate magma ascent.

On another hand, the trajectory followed by ascending magmatic intrusions is strongly influenced by the crustal stress field (Lister, 1990, 1991; Weertman, 1971). In particular, the unloading due to the crater topography generates a specific stress state such that the least compressive stress is vertical while the maximum compressive stress is horizontal below the crater topography (Maccaferri et al., 2014; Michaut et al., 2020). As tensile fractures

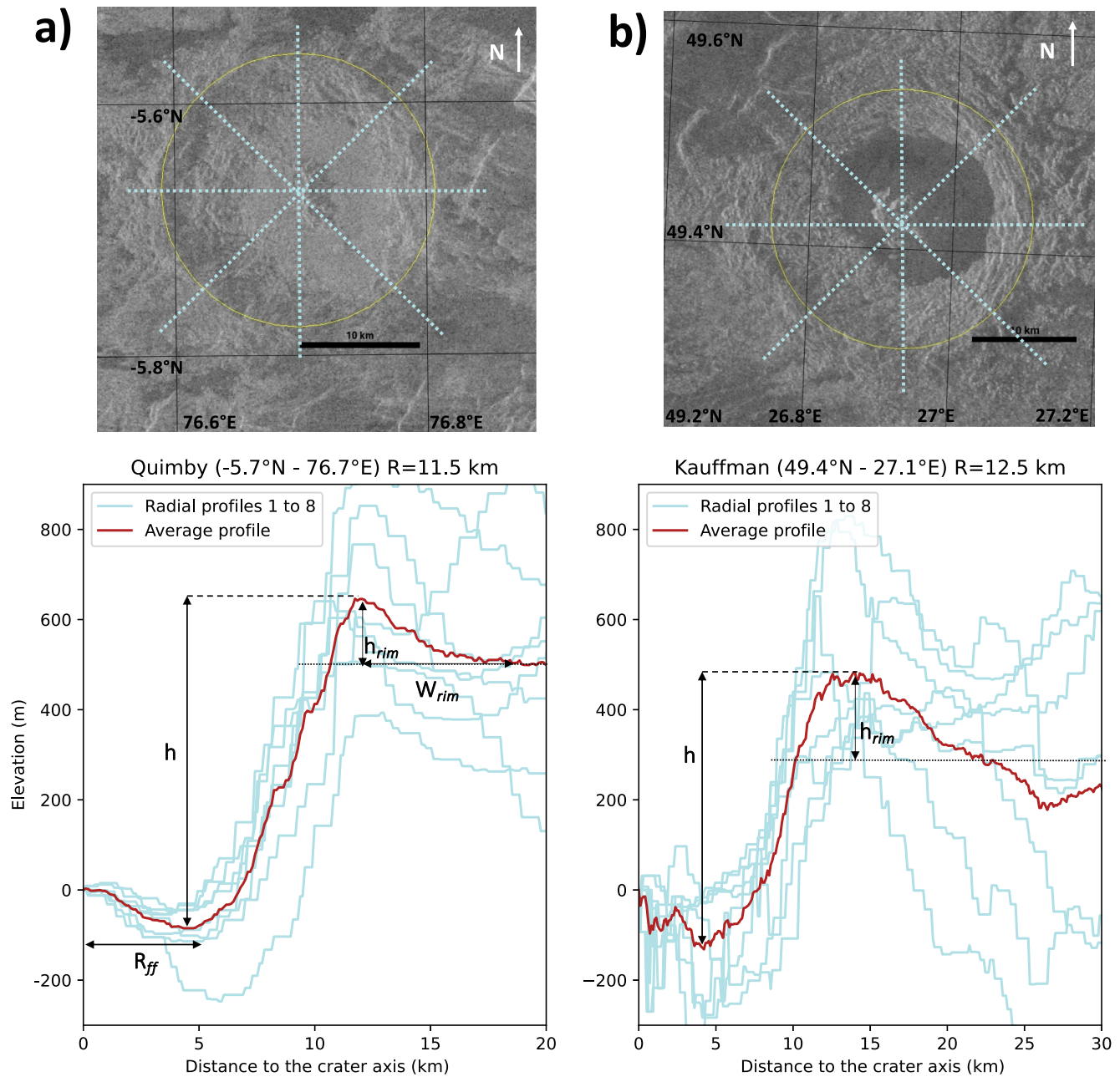


Figure 2. Two examples of craters: (a) Quimby a bright-floored crater and (b) Kauffman a dark-floored. Top: Magellan Synthetic Aperture Radar images and profiles drawn from JMars. Bottom: topographic profiles obtained from the stereo map of Venus (in blue) (Herrick et al., 2012) with the average profile derived from these data (in red) and the measured depth of crater h , the rim height h_{rim} , the rim width W_{rim} and the flat floor radius R_{ff} for Quimby crater. Rim height corresponds to the difference between the highest point of the rim (dashed line) and the level of the surrounding terrain (dotted line) at 3 radii of the crater center as in Herrick et al. (1997).

are preferentially oriented in the plane perpendicular to the direction of least compressive stress, the stress state resulting from a surface unloading tends to horizontalize vertical magma-filled cracks propagating upwards below the crater (Corbi et al., 2016; Maccaferri et al., 2014; Pinel et al., 2017). During the last few decades, analogic and numerical modeling were both used to understand how the magma driving pressure and crustal stress state influence the magma path in the crust (Rivalta et al., 2015). It was shown that the deflection of vertically propagating dykes depends on how their driving pressure compares to the local shear stress on a vertical dyke (Maccaferri et al., 2019), with a large driving pressure favoring a straight ascent toward the surface and a large shear stress gradient favoring deviation in the direction of the maximum compressive stress. In the Highlands of the Moon, where the crust is thick and of low density (on average $2,550 \text{ kg m}^{-3}$), magma tends to store at shallow

depths below craters in the form of horizontal sills or laccoliths (Jozwiak et al., 2012; Schultz, 1978; Thorey & Michaut, 2014; Thorey et al., 2015; Wieczorek et al., 2013), where dyke horizontalization can be caused by the stress state induced by the crater unloading (Michaut et al., 2020). Contrastingly, in the crustal plateaus of Venus, observations suggest that magma can erupt, in particular on the crater floor.

We first gather quantitative observations on a set of craters located in the crustal plateaus. Using the typical topography of bright-floored craters, we construct the elastic stress state in the crust resulting from a fresh crater topography. Then, we use a boundary element (BE) model to investigate the trajectory of magmatic dykes in the crater-induced stress field depending on the crust and magma properties. Our numerical results show four different types of behavior for magmatic intrusions, including one where magma only erupts in the crater interior and remains stored in the crust outside of it. Based on dimensionless numbers characteristic of the physics of our problem, we construct a regime diagram which allows to constrain the crust and magma properties specific to this behavior.

2. Observations on a Set of Craters

2.1. Rim-Floor Depth and Rim Height

Previous works by Sharpton (1994), Herrick and Sharpton (2000), and Herrick and Rumpf (2011) studied and compared the morphologies of bright and dark-floored craters, but mainly for craters located in the plains of Venus. Here, we study the topography of dark-floored craters located in the tessera plateaus because, in the highly deformed terrains constituting the tesserae, resurfacing seems to mainly occur within craters (see for instance the dark volcanic floors of craters Chloe and Kauffman that contrasts with the highly deformed surrounding terrains, Figure 1). We also restrict our study to dark-floored craters located at large elevations, that is, >1 km above the mean planet radius because the topography on Venus is likely correlated to the crust thickness, which has a large influence on the ability of negatively buoyant magma to reach the surface. We compare the topography of these dark-floored craters to that of bright ones located in the same areas. Since bright-floored craters have not been modified and as the number of craters in the tesserae plateaus is limited, we enlarge our bright-floored crater data set by considering those located in other topographic highs (i.e., >1.5 km above the mean planet radius) than tesserae terrains (Figure 3).

While several crater databases exist for Venus (Campbell et al., 1992; Schaber et al., 1992), we use that of Herrick et al. (1997) as it provides a number of useful parameters for this study such as the crater floor reflectivity (bright, dark or indeterminate, the latter referring to craters that cannot be classified as bright or dark) and the elevation of the surrounding terrain. This database is also available on JMars, which was used to determine the crater topographic profiles. Our selected craters are located in Ishtar Terra and Aphrodite Terra, specifically in Ovda and Thetis Regios as well as in Fortuna Tessera and Tellus Regio (Figure 3).

A total of 22 craters were studied using the Magellan SAR data, including 8 dark-floored craters and 14 bright-floored ones (Table 1, Figure 3).

For each crater, eight radial topographic profiles (in blue on Figure 2), considering a 45° step between each of them, were drawn using the JMars software developed by Christensen et al. (2009) from which we deduce the average crater topography (red profile in Figure 2). From the average profile, we measure the crater rim-floor depth, which is the difference between the top of the rim and the crater floor (Figure 2). When available, we use the stereo-derived topographic map developed by Herrick et al. (2012) with horizontal and vertical resolutions of ≈ 1 km and ≈ 100 m, respectively, but that covers only $\approx 20\%$ of the surface. Craters for which the resolution was not good enough were discarded. For eight useable craters located in areas without stereo coverage, the topography was extracted from the Global Topographic Data Record collected by the Magellan mission, for which the horizontal resolution is at least an order of magnitude less than the stereo (Ford & Pettengill, 1992; Herrick et al., 2012).

The results (Figure 4a) clearly show that for both populations, the crater depth $h_{\text{bright/dark}}$ increases with the radius, with each population following a different power law, similarly to what has been previously found in the volcanic plains (Herrick & Rumpf, 2011; Herrick & Sharpton, 2000; Sharpton, 1994). Despite the rather small number of available craters and the large error bars overlapping the power law for bright-floored craters, the dark-floored craters are systematically located below this power law, in agreement with volcanic infilling of the crater interior.

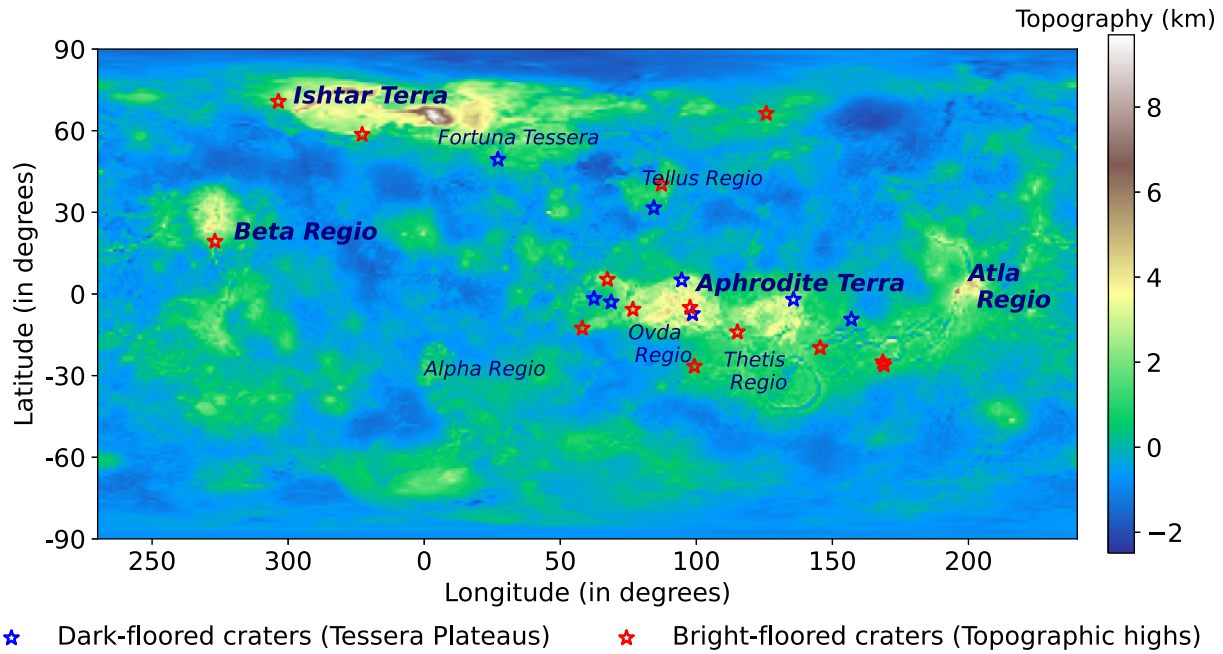


Figure 3. Location of the selected bright-floored craters (red stars) in the topographic highs and dark-floored craters (blue stars) used in this study. Studied dark-floored craters are located in the main tessera plateaus: Aphrodite Terra, which includes Onda and Thetis Regios, Fortuna Tessera, and Tellus Regio, as indicated on this map. Topography is given with respect to the mean planetary radius (6,051 km). Map retrieved from the NASA Planetary Database Geosciences Node (<https://pds-geosciences.wustl.edu/missions/magellan/index.htm>).

We use a least-square fit to determine a power law relationship between the rim-floor depth $h_{\text{bright/dark}}$ and the diameter D , both expressed in kilometers, for each crater population:

$$h_{\text{bright}} = 0.376 D^{0.197}, \quad (1)$$

$$h_{\text{dark}} = 0.413 D^{0.092}. \quad (2)$$

where $h_{\text{bright/dark}}$ is a positive quantity. In comparison, the power laws obtained for the two types of craters in the plains are (Herrick & Rumpf, 2011):

$$h_{\text{bright}}^p = 0.483 D^{0.165}, \quad (3)$$

$$h_{\text{dark}}^p = 0.424 D^{0.108}, \quad (4)$$

where superscript p stands for plains.

Herrick and Rumpf (2011) showed that dark-floored craters in the plains generally present shorter rims than bright-floored ones, suggesting that volcanic resurfacing occurred both outside and inside craters there. This is not the case for our set of craters; there appears to be no difference in rim heights in between the two crater populations (Figure 4b), which argues in favor of volcanic infilling inside the crater only in the crustal plateaus.

Considering that dark-floored craters have indeed undergone volcanic filling by lava (Herrick & Phillips, 1994; Herrick & Rumpf, 2011; Wichman, 1999), we estimate the magma-filling thickness inside the crater Δh from:

$$\Delta h = h_{\text{bright}} - h_{\text{dark}} \quad (5)$$

As noted by Wichman (1999), both the rim-floor depth and the filling thickness Δh increase with crater radius (Figures 4a and 4c). The magma filling thickness Δh appears in general lower (by ~30% on average) for craters in

Table 1
List of Impact Craters Used in This Study and Their Characteristics

Name	Latitude (°N)	Longitude (°E)	Region	Category	Diameter (km)	Elevation (km)	Depth (m)	Error on depth (m)	Source	Tessera plateaus
Andreianova	−3.0	68.7	Ovda Regio	Dark	69.5	6,053.00	573	375	ST	Yes
Austen	−25.0	168.5	Aphrodite Terra	Bright	43.9	6,052.50	743	408	MA	No
Bernhardt	31.6	84.4	Tellus Regio	Dark	25.0	6,052.00	486	215	ST	Yes
Blanche	−9.3	157	Thetis Regio	Dark	11.8	6,053.00	535	24	ST	Yes
Boulanger	−26.6	99.3	Ovda Regio	Bright	73.7	6,052.60	721	346	MA	Yes
Carter	5.3	67.3	Ovda Regio	Bright	19.3	6,054.10	650	211	ST	Yes
Chloe	−7.3	98.6	Ovda Regio	Dark	17.8	6,055.90	550	50	ST	Yes
Cotton	70.7	300.2	Ishtar Terra	Bright	47.8	6,053.00	805	63	MA	No
Halle	−19.8	145.5	Thetis Regio	Bright	21.1	6,053.00	686	150	ST	Yes
Hepworth	5.1	94.6	Ovda Regio	Dark	62.5	6,054.20	704	362	ST	Yes
Janina	−2	135.7	Thetis Regio	Dark	9.3	6,053.30	510	20	ST	Yes
Joliot-Curie	−1.7	62.4	Ovda Regio	Dark	100.9	6,052.50	614	462	ST	Yes
Kauffman	49.4	27.1	Fortuna Tessera	Dark	25.0	6,053.00	560	48	ST	Yes
Khatun	40.3	87.2	Tellus Regio	Bright	42.4	6,052.60	830	406	ST	Yes
Magnani	58.6	337.2	Fortuna Tessera	Bright	26.4	6,053.50	740	323	MA	Yes
Quimby	−5.7	76.7	Ovda Regio	Bright	22.9	6,054.20	725	140	ST	Yes
Recamier	−12.6	58.1	Ovda Regio	Bright	25.5	6,052.70	955	462	ST	Yes
Salika	−5.0	97.7	Ovda Regio	Bright	12.0	6,055.50	562	183	ST	Yes
Weil	19.3	283.1	Beta Regio	Bright	23.4	6,053.90	674	211	MA	No
Yasuko	−26.1	169.0	Thetis Regio	Bright	10.5	6,053.10	541	117	MA	Yes
Yonge	−14.0	115.1	Thetis Regio	Bright	32.1	6,053.80	749	139	MA	Yes
Zhilova	66.3	125.7	Ishtar Terra	Bright	53.3	6,052.50	875	376	MA	No

Note. Data were obtained using Herrick's crater database (Herrick et al., 1997). Latitude and longitude are given for the center of the crater. The elevation is that of the surrounding terrain, measured at three radii from the crater center. Topographic profiles and rim-floor depths were obtained using JMARS (Christensen et al., 2009). Two topographic sources are used: the Magellan altimetry (MA) and the Magellan Stereo Topography (ST). Bright-floored craters located outside the Tessera plateaus serve as a mean of minimizing the error on the rim-floor depth power law. Average height for Aphrodite Terra and Ishtar Terra is 3,000 m above the mean planetary radius.

the crustal plateaus than for craters in the plains (Figure 4c), which is another argument showing that volcanic resurfacing is much more limited in the tesserae.

2.2. Characteristic Topography for a Fresh Crater

From observations on bright-floored craters, we construct a standard topographic profile in axisymmetric geometry $h(r)$ for a pristine crater, where r is the radial coordinate and $h(r)$ is negative when the topography is below the far field value. This profile is then used to compute the unloading stress field in the underlying elastic medium, where the vertical axis z is then oriented downwards (Section 3.1). As in Michaut and Pinel (2018), we consider a typical truncated cone-shaped crater with a flat floor at the bottom, where the flat floor radius R_{ff} is a fraction f_f of the crater radius (Figure 5). In addition, we consider the presence of a rim of height h_{rim} and width W_{rim} that both vary with the crater radius (Figure 5). We determine the radius dependency of these three quantities (R_{ff} , h_{rim} , and W_{rim}) based on our observations on bright-floored craters (see Supporting Information S1) for which we have good quality topographic profiles from the stereo map (Figures 2 and 5) and set them as follows:

- $R_{ff} = f_f R$ with $f_f = 40\%$,
- $h_{rim} = f_r h_{bright}$ with $f_r = 35\%$ (note that h_{bright} is itself function of the crater radius through Equation 1),
- $W_{rim} = f_{wr} R$ with $f_{wr} = 40\%$.

With these considerations, we obtain:

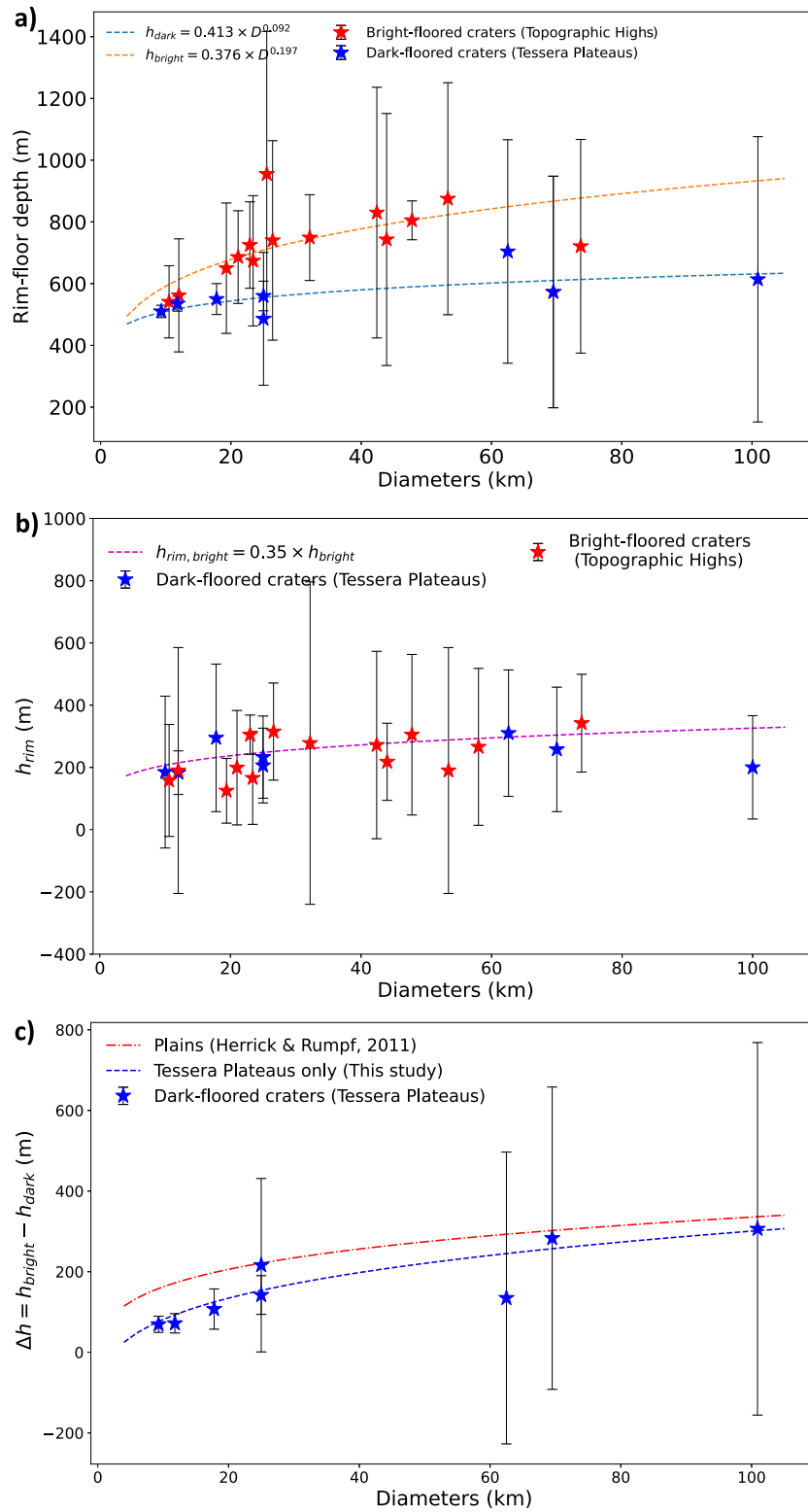


Figure 4.

$$\begin{aligned}
 h(r) &= -(h_{\text{bright}} - h_{\text{rim}}) \quad 0 \leq r \leq f_f R \\
 h(r) &= h_{\text{bright}} \times \frac{r - R}{R - f_f R} + h_{\text{rim}} \quad f_f R \leq r \leq R \\
 h(r) &= h_{\text{rim}} \times \left(1 - \frac{r - R}{W_{\text{rim}}}\right) \quad R \leq r \leq R + W_{\text{rim}} \\
 h(r) &= 0 \quad r \geq R + W_{\text{rim}}
 \end{aligned} \tag{6}$$

3. Modeling Magma Propagation in an Existing Stress Field

In this study, an elastic rheology is assumed for the crust. On Venus, viscous or viscoelastic behavior of the crust is often assumed when studying crustal topographic relaxation (Nimmo & Mackwell, 2023) or crustal deformation induced by mantle circulation and flow (Gerya, 2014), which are processes occurring over timescales of million years to gigayears. Here we are interested in magma propagation in the crust in the form of dykes, giant dyke swarms being observed on both Venus and the Earth (Ernst et al., 1995; Grosfils & Head, 1994). Dyke propagation occurs over short timescales: on Earth, geophysical observations indicate ascent duration of several hours to several days (Aoki et al., 1999; Battaglia et al., 2005; Beauducel et al., 1999; Peltier et al., 2005, 2007). On such timescales, viscoelastic effects are generally negligible, and numerical models simulating the propagation path of magma-filled dykes mostly rely on the assumption of a brittle-elastic rheology (Rivalta et al., 2015). Additionally, observations of faults and grabens in the crustal plateaus testify of their elastic-brittle behavior (Ghent & Hansen, 1998; Gilmore et al., 1994).

3.1. Stress Field Caused by a Crater Topography

The stress field within the crust due to a topography $h(r)$ can be calculated using a surface load $P_h(r) = \rho_c g h(r)$, which can be positive or negative depending on the surface topography. The elastic stress components resulting from an axisymmetric load at the surface of a semi-infinite elastic medium are given by Sneddon (1951):

$$\sigma_{rr} = \int_0^\infty (1 - z\xi)Z(\xi)e^{-\xi z}J_0(\xi r) d\xi + \frac{1}{r} \int_0^\infty Z(\xi) \left(z - \frac{\mu}{(\lambda + \mu)\xi} \right) e^{-\xi z} J_1(\xi r) d\xi, \tag{7}$$

$$\sigma_{zz} = z \int_0^\infty Z(\xi)e^{-\xi z}J_0(\xi r)\xi d\xi + \int_0^\infty Z(\xi)e^{-\xi z}J_0(\xi r) d\xi, \tag{8}$$

$$\sigma_{\theta\theta} = \frac{\lambda}{\lambda + \mu} \int_0^\infty Z(\xi)e^{-\xi z}J_0(\xi r) d\xi - \frac{1}{r} \int_0^\infty Z(\xi) \left(z - \frac{\mu}{(\lambda + \mu)\xi} \right) e^{-\xi z} J_1(\xi r) d\xi, \tag{9}$$

$$\sigma_{rz} = z \int_0^\infty Z(\xi)e^{-\xi z}J_1(\xi r)\xi d\xi, \tag{10}$$

$$\sigma_{r\theta} = \sigma_{\theta z} = 0, \tag{11}$$

where

$$Z(\xi) = -\xi \int_0^\infty r P_h(r) J_0(\xi r) dr. \tag{12}$$

Figure 4. (a) Rim-floor depth as a function of diameter for our selected set of bright-floored and dark-floored craters and associated power law relationships (orange dashed line from Equation 1 and light blue dashed line from Equation 2). (b) Rim height as a function of crater diameter. (c) Depth difference $\Delta h = h_{\text{bright}} - h_{\text{dark}}$ between bright-floored and dark-floored craters as a function of crater diameter for craters in the plains (red dash-dotted line determined from Equations 3 and 4) and in the plateaus (blue dashed line from Equations 1 and 2). Blue stars correspond to the depth difference between that of bright-floored craters from the power law relationship (Equation 1) and the observed depth of the dark-floored craters in the plateaus. In all plots, blue symbols represent dark-floored craters and red symbols represent bright-floored ones. On (a) and (b), error bars represent the standard deviation estimated from the eight radial topographic profiles of each crater.

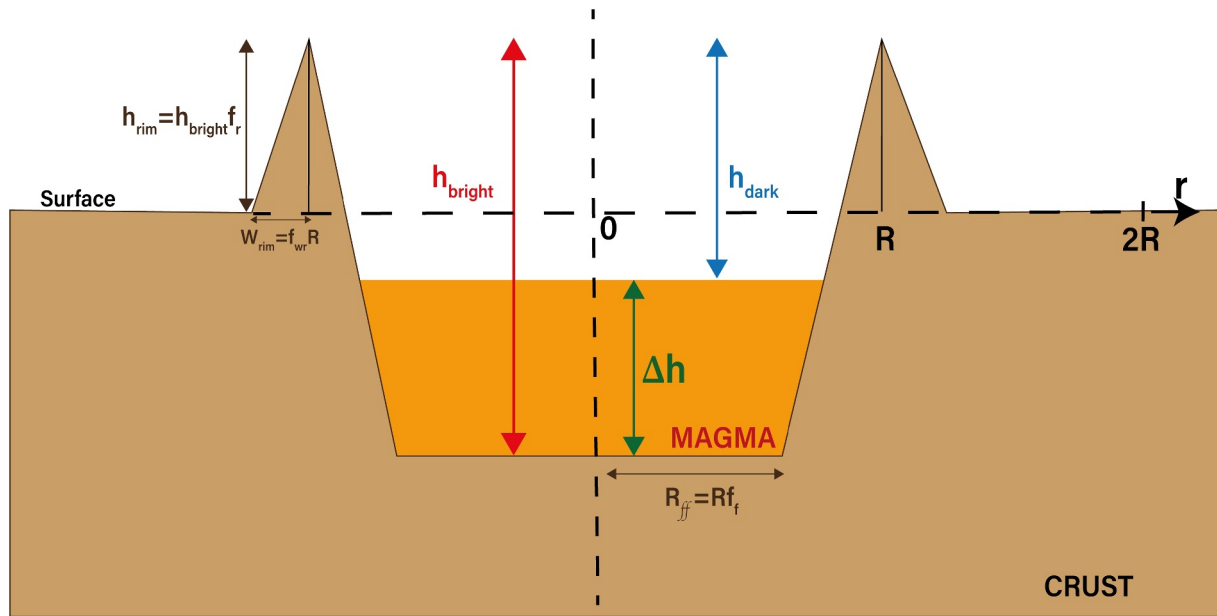


Figure 5. Schematic of a truncated cone-shaped crater with a rim. The thickness of the partial infilling of a crater by lavas Δh , corresponding to the difference in depth between bright-floored and dark-floored craters $h_{\text{bright}} - h_{\text{dark}}$, is represented. Quantities h_{rim} , R_{ff} and W_{rim} are also represented.

J_0 and J_1 are the Bessel functions of order zero and one respectively, μ the shear modulus, λ the Lamé coefficient (Table 2), and r, θ, z are the cylindrical coordinates with z oriented downwards. The stress components σ_{ij} , where $i, j = r, \theta, z$, are considered positive in tension. The pressure perturbation due to the crater unloading is calculated from:

$$P(r, z) = -\frac{\sigma_{rr} + \sigma_{\theta\theta} + \sigma_{zz}}{3}. \quad (13)$$

We compute the stress field components using a Matlab code (Le Contellec, 2024a, description provided as a Supporting Information S1) for $R = 5, 10, 15,$ and 20 km, over 3 – 10 radii in radial coordinates r as well as in depth z . Values of the parameters used to calculate the stress field are given in Table 2. The stress perturbation vanishes over a characteristic depth similar to the crater radius (Figure 6).

We note σ_3 and σ_1 the smallest and largest compressive principal stresses in the r, z plane. At the axis of the unloading, $\sigma_3 = \sigma_{zz}$, and $\sigma_1 = \sigma_{rr}$. Such a configuration favors the horizontal orientation of magma filled cracks (Cotterell & Rice, 1980; Michaut et al., 2020), in particular if the magma driving overpressure is small. Both the radial and vertical stresses σ_{rr} and σ_{zz} are maximum at the surface, and the non-diagonal stress σ_{rz} is maximum at depth $z \approx R/2$ and $r \approx 2R/3$ (Figure 8).

3.2. Magma-Filled Crack Propagation in an Existing Stress Field

3.2.1. Description of the Model

We study the effect of the stress field caused by a crater topography on the ascent of an initially vertical magma dyke, as a function of crater radius, magma and encasing rocks properties, particularly crust, mantle and magma densities. The available melt is not resulting from the impact itself but likely comes from decompression melting caused by mantle convection. Melting resulting from the impact process is only significant for craters far greater in size than the one studied here (B. Ivanov & Melosh, 1995; Manske et al., 2021).

To model dyke ascent, we use the BE model of dyke propagation in an external stress field developed by Maccaferri et al. (2011); this model is thoroughly described in Maccaferri et al. (2010, 2011, 2019). We thus provide only a short description of the model and refer to the literature cited above for more details.

Table 2
List of Parameters of the Model

Parameters	Symbols	Values
Crater geometry parameters		
Radius	R	5–20 km
Crater topographic profile	h	
Crater depth	h_{bright}	592–778 m
Fraction of flat floor	f_f	0.4
Fraction of rim height	f_r	0.35
Fraction of rim width	f_{wr}	0.4
N	Number of points sampled across r and z	496–597
N_b	r and z extension of the stress field	3–10
Numerical models parameters		
Gravity	g	8.87 m s ⁻²
Lamé coefficient	λ	4 × 10 ¹⁰ Pa
Shear modulus	μ	4 × 10 ¹⁰ Pa
Initial depth (Mantle–Crust transition)	D_i	10–47 km
Mantle density	ρ_{mant}	3,300 kg m ⁻³
Crust density	ρ_c	2,385–3,007 kg m ⁻³
Magma density	ρ_{mag}	2,650–3,100 kg m ⁻³
Density difference between crust and magma	$\Delta\rho_c = \rho_{\text{mag}} - \rho_c$	0–300 kg m ⁻³
Density difference between mantle and magma	$\Delta\rho_m = \rho_{\text{mant}} - \rho_{\text{mag}}$	200–650 kg m ³
Dislocation element length	l	100 m
Number of dislocation elements	n	90–207
Initial crack length	L	9–20.7 km
Normalized crack length	$L^* = \frac{L}{D_i}$	0.35–2
Magma initial overpressure (buoyancy)	ΔP_i	6–21 MPa

Note. The first part presents the parameters used to calculate the unloading stress field. The second part concerns the parameters used to compute the dyke propagation model.

The model is 2D (plane strain approximation) and assumes a linearly elastic, isotropic medium stratified in density with the possibility of introducing an elastic heterogeneity, such as the crust-mantle boundary, for instance. For simplicity, we consider the same elastic parameters for the crust and mantle $\mu = \lambda = 40$ GPa. We set the crust density ρ_c , over a crustal thickness D_i , to a smaller value than the mantle density ρ_{mant} (Figure 7). The magma, of density ρ_{mag} , is positively buoyant in the mantle, and negatively buoyant in the crust, that is, $\rho_c \leq \rho_{\text{mag}} \leq \rho_{\text{mant}}$, and we note $\Delta\rho_m = \rho_{\text{mant}} - \rho_{\text{mag}}$ and $\Delta\rho_c = \rho_{\text{mag}} - \rho_c$, both quantities being positive.

The dyke is modeled as a boundary-element crack of initial length L set as input, and is composed of n interacting dislocation elements (DE) of length l , such that $L = n \times l$. The crack propagates through the host rocks by incremental elongation (opening new DE) in the direction that maximizes the strain and gravitational energy release. Propagation of the dyke is allowed when the energy release, that is the sum of the strain and gravitational energies, exceeds the fracture energy E_f , which is a function of the host rocks fracture toughness. For simplicity and in order to focus on the effect of magma and crust properties on dyke propagation, we consider a null fracture toughness ($E_f = 0$). Simulations considering a characteristic fracture toughness for crustal rocks of 100 MPa (Rivalta et al., 2015) showed no difference in propagation path for the dykes than the cases of null fracture toughness. The direction of dyke elongation is defined by the competition between the internal magma pressure and external stresses, the latter being the sum of the lithostatic pressure $\int_0^z \rho(z)gz$ and the topographic stress field, both being given at the center of each dislocation element. The overpressure profile along the dyke is the

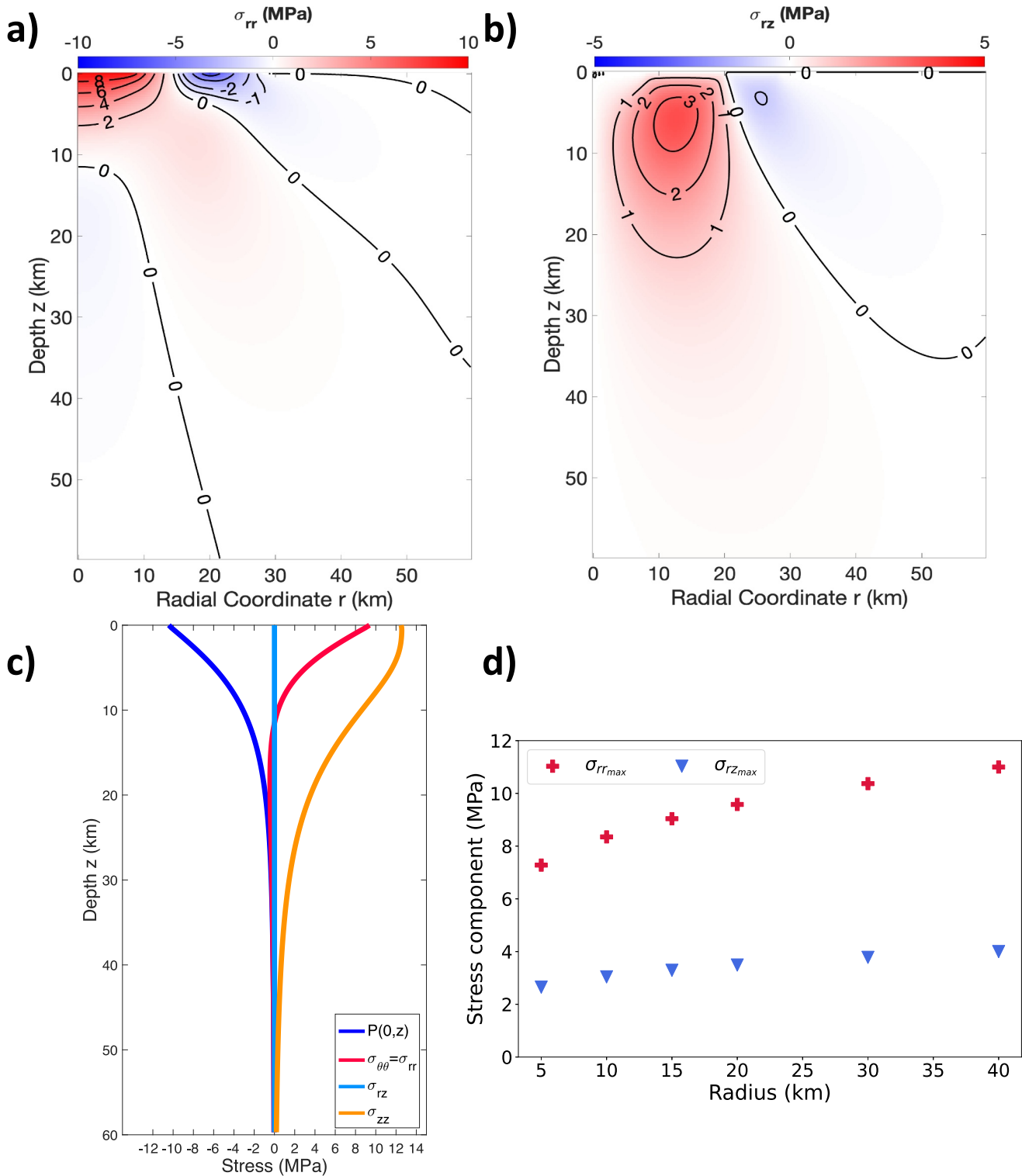


Figure 6. Radial and non-diagonal stress perturbations σ_{rr} and σ_{rz} caused by a crater unloading of topography $h(r)$ (Equation 6) at the surface of a semi-infinite medium, with $R = 20$ km and $h_{\text{bright}} = 780$ m. Tension is positive. (a) Radial stress σ_{rr} , varying between -2 and 9 MPa. (b) Shear stress on the coordinate planes σ_{rz} , varying between -1 and 4 MPa. (c) Stress components $\sigma_{rr}(0, z)$, $\sigma_{rz}(0, z)$, $\sigma_{\theta\theta}(0, z)$, $\sigma_{zz}(0, z)$, and pressure perturbation $P(0, z)$ at the axis of the unloading. (d) Maximum values of σ_{rr} (red crosses) and σ_{rz} (blue triangles) for crater radii ranging from 5 to 40 km. The ratio $\sigma_{rz_{max}}/\sigma_{rr_{max}}$ remains approximately constant and equal to 0.36 while varying the crater radius. The parameters used to calculate this stress field are given in Table 2.

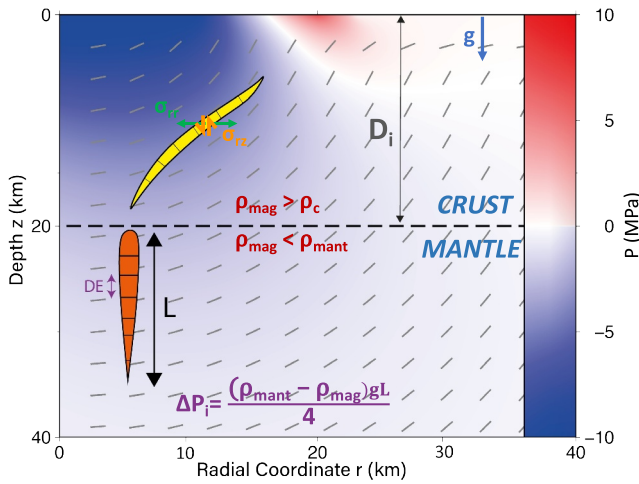


Figure 7. Schematic for the dyke propagation model in an external stress field adapted from Maccaferri et al. (2011). The dyke of length L is composed of a succession of n dislocation elements of length l . This model considers the stress balance at the center of each of these elements to test for dyke propagation. The different stress components σ_{rr} and σ_{zz} acting on the opening/closing and deviation of the dyke are represented. The color scale represents the pressure perturbation caused by the unloading (a crater topography of radius $R = 20$ km in that case) and the dashes exterior to the cracks, the direction of the maximum compressive stress σ_1 . The dyke initially starts in the mantle with an overpressure ΔP_i (orange dyke) and propagates until it reaches its final state (yellow dyke). The case of a crack starting at the lateral position $R/4$ is represented.

difference between the fluid pressure and the normal component of the external stress acting on each dislocation element.

The topographic stress field is calculated from Equations 7–12 for a crater topography (Equation 6) in an axisymmetric geometry with a spatial discretization of 100 m. We verified that a smaller discretization gives the same dyke propagation path. The dyke propagation code is in a plane strain configuration while our stress state is 3D. However, we show that $\sigma_3 > \sigma_{\theta\theta}$ almost everywhere below the crater; thus the most extensive principal stress lies almost everywhere in the r, z plane, which justifies the 2D computation (see Supporting Information S1). The region where this is not verified is limited and close to the surface; it should not change our conclusions on dyke deviation. We therefore only use the stress components σ_{rr} , σ_{zz} , and σ_{rz} . Furthermore, by symmetry, the only non-vanishing non-diagonal stress is σ_{rz} .

The dyke is initially located in the mantle, where the magma is assumed buoyant. Although the model makes it possible to account for magma compressibility, to focus on the effects of crater unloading and magma buoyancy we use a very large bulk modulus for the magma of 500 GPa, mimicking the behavior of an incompressible magma. In a 2D isotropic elastic medium, a vertical crack filled by buoyant and incompressible magma tends to a quasi-static shape (tear drop shape) with null stress intensity factor at the lower tip of the crack, and a length L , equal to the Weertman length, such that the initial average overpressure within the dyke is (Weertman, 1971):

$$\Delta P_i = \frac{\Delta \rho_m g L}{4}. \quad (14)$$

We start with a dyke at this initial length L in the mantle (which is set from a chosen 2D volume V in the propagation code). This initial length is defined in absence of a topographic stress field and, in that case, the initial magma driving pressure ΔP_i is given by Equation 14. We start with a dyke tip located at the crust-mantle interface, that is, at a depth D_i . Starting with a deeper dyke makes negligible differences on the propagation path followed by a dyke as (a) we start at the quasi-static length L in absence of an unloading stress field, hence the dyke overpressure would be unchanged, (b) the large density difference between the magma and the mantle imposes a rather large initial fluid overpressure, making it insensitive to the deviatoric stress potentially caused by a crater, in particular since the non-diagonal shear stress vanishes with depth.

During each simulation, as the dyke intrudes within the crust, where the buoyancy is reduced and the stress field is heterogeneous, the dyke length, shape, and orientation change. Eventually, the dyke will reach the surface (within or outside the crater), or gets stuck at depth, depending on magma buoyancy, crust properties, and crater geometry. For each run, we simulate the ascent of 6 dykes, from different positions, that do not interact with each other. Even though a propagating dyke locally changes the stress state on the path it follows, we set the model so that each dyke is only sensitive to the external stress field, and not to the stress perturbation caused by the other dykes. One dyke is always positioned at 1 km of the axis; the other dykes are positioned at $R/4$, $R/2$, $2R/3$, R , and at $2R$. The one located at $2R$ serves as a “control dyke,” meaning it gives us the propagation path a dyke would have followed in absence of an external stress caused by the crater topography.

3.2.2. Parameters and Dimensionless Numbers of the Model

The parameters controlling the outcome of a numerical simulation (whether or not a dyke erupts, and where) are the crater radius R , which controls the crater topography and the amplitude of the resulting stress field and stress components, the crust, magma and mantle densities, ρ_c , ρ_{mag} , and ρ_{mant} , which set the magma buoyancy in the two different layers, the initial dyke length L , corresponding to a given initial volume V , and the crust thickness D_i (Table 2).

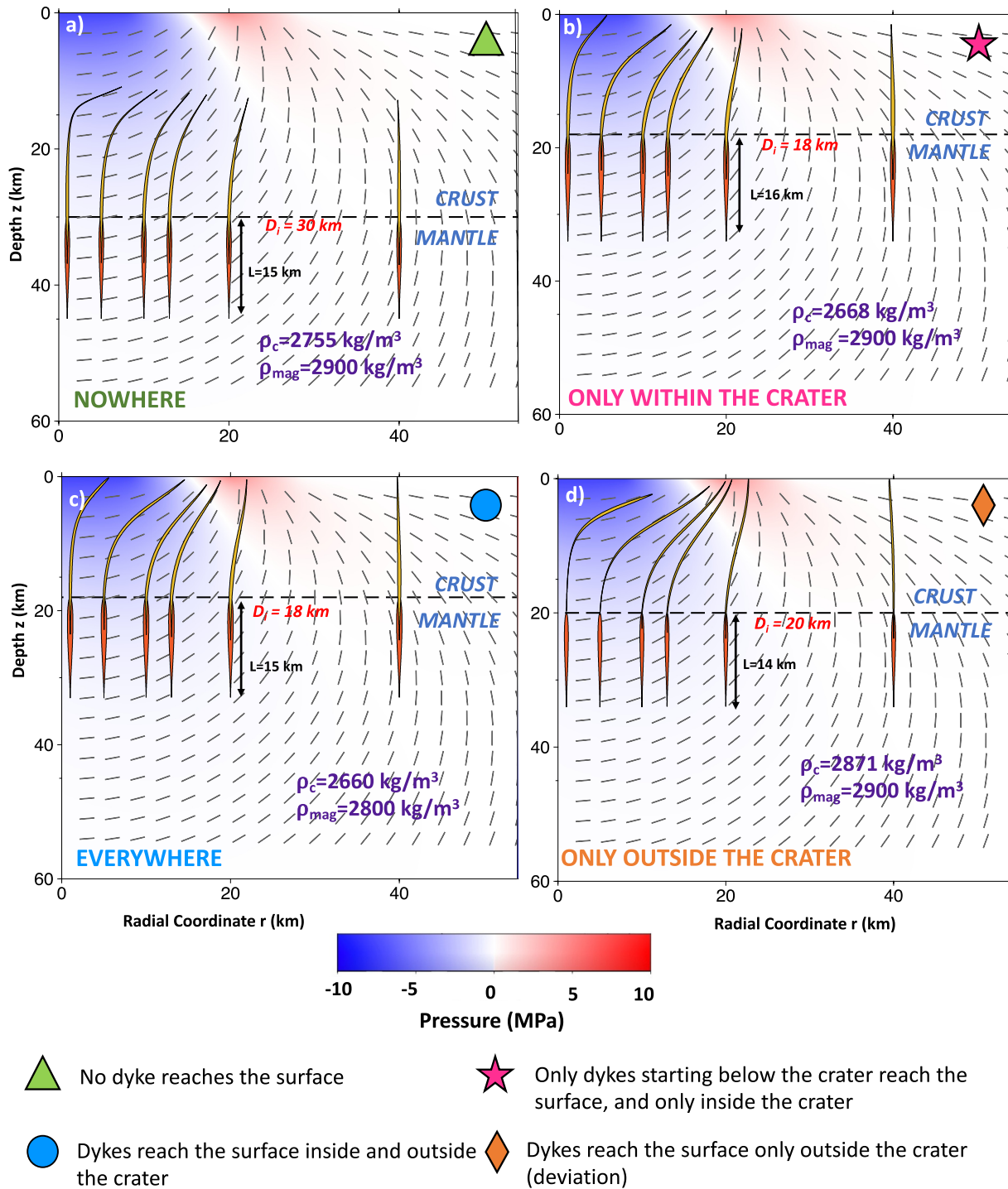


Figure 8. Four typical propagation behaviors for magma-filled cracks below a crater of radius $R = 20 \text{ km}$. For each example, two dykes are represented: the initial state with the upper tip at the crust/mantle transition (orange dyke), and the final stage of the dyke when its propagation is complete (yellow dyke). The dykes can either remain stored at depth (green triangles), reach the surface only within the crater (pink stars), reach the surface both inside and outside the crater (blue dots) or reach the surface only outside the crater (orange diamonds). Several parameters vary: initial depth D_i , crust density ρ_c , magma density ρ_{mag} and the initial length of the dyke L . Gray dashed lines indicate the direction of maximum compressive stress σ_1 and background color-scale is the pressure perturbation caused by the unloading P (MPa). Values of E , μ , λ , and g used for these simulations are given in Table 2.

The stress field due to the crater topography has two different effects on the path followed by a dyke. Below the crater, the radial stress σ_{rr} increases toward the surface (Figures 6a–6c), and tends to facilitate the opening and upward propagation of a vertical magma filled crack rising below the crater (Michaut & Pinel, 2018; Walwer et al., 2021). On the contrary, the shear stress $\sigma_{rz_{\max}}$ tends to deviate magma ascent from its vertical path (Dahm, 2000; Watanabe et al., 2002), favoring, when the magma driving pressure is low, its deflection toward the direction of σ_1 , a full deflection leading to horizontal crack opening below the crater center (Figure 7 and Figure S2 in Supporting Information S1) (Maccaferri et al., 2019). Both σ_{rr} and σ_{rz} increase with the crater radius (Figure 6d). For each crater radius R , we quantify these two effects using the maximum values of these two stress components $\sigma_{rr_{\max}}$ and $\sigma_{rz_{\max}}$.

The initial dyke overpressure ΔP_i (Equation 14), which depends on the density contrast between the magma and the mantle and on the initial dyke length L , provides the overpressure needed for the dyke to intrude and propagate through the crust, where magma buoyancy is negative. This last effect is quantified by the pressure scale $\Delta\rho_c g D_i$.

We thus have four characteristic pressure scales acting differently on dyke propagation: ΔP_i and $\sigma_{rr_{\max}}$ both favor vertical magma ascent, while $\Delta\rho_c g D_i$ impedes vertical ascent and $\sigma_{rz_{\max}}$ favors deviation.

We first define two dimensionless numbers as ratios of two characteristic pressure scales representing two competing mechanisms on the vertical ascent of a dyke:

$$\Gamma = \frac{\sigma_{rr_{\max}}}{\Delta\rho_c g D_i}, \quad (15)$$

$$\Lambda = \frac{\Delta P_i}{\Delta\rho_c g D_i}. \quad (16)$$

Additionally, for given dyke overpressure and external stress, longer dykes are less prone to deflection (Maccaferri et al., 2019). The deeper the dyke starts, that is, the larger D_i , the more room it has to deviate from its vertical trajectory. As in Maccaferri et al. (2019), we introduce the dimensionless initial length of the dyke expressed as:

$$L^* = \frac{L}{D_i}, \quad (17)$$

where larger L^* should facilitate vertical propagation and inversely.

On the other hand, magma deviation is facilitated by larger values of the shear stress on the initially vertical dyke, scaling with $\sigma_{rz_{\max}}$, and by large dyke depth scaling with D_i . Dyke deviation is on the contrary hindered by large driving pressures for the dyke, scaling with ΔP_i , and large dyke lengths L . Following Maccaferri et al. (2019), we introduce, in addition to L^* , the dimensionless number δ defined as:

$$\delta = \frac{\sigma_{rz_{\max}} D_i}{\Delta P_i L}, \quad (18)$$

which is the ratio between parameters favoring deviation over parameters impeding it. The lower the value of δ , the less a dyke is deflected by the external stress, and vice versa.

We are interested in studying which conditions allow the magma to reach the surface exclusively inside an impact crater. For that to occur, the dyke must (a) ascend up to the surface and (b) not be deviated at depth below the crater and not reach the surface beyond the rim. Thus, while large values of Γ , Λ , and L^* should favor vertical ascent up to the crater floor, large values of δ should on the contrary favor horizontal dyke deviation below the crater.

4. Results

We ran a set of 107 simulations of dyke propagation for various crater radius R , initial depth D_i , density contrasts between the magma and crust $\Delta\rho_c$ and between the mantle and magma $\Delta\rho_m$, and initial dyke length L (see Table 2).

Four different behaviors are identified, depending on whether or not the dykes reach the surface and where (within or outside the crater). Examples of these behaviors are shown on Figure 8: the dykes can either remain stored at depth (green triangles), reach the surface only within the crater (pink stars), reach the surface everywhere, meaning both inside and outside the crater (blue dots) or reach the surface only outside the crater (orange diamonds).

We first analyze the behavior of the “control dykes,” which are the dykes starting at a distance $r = 2R$ from the crater axis, far enough from the crater for its stress field to be negligible and for these dykes not to be deviated. These dykes can thus either get stuck within the crust, or reach the surface outside the crater. On a $\Gamma(\delta)$ diagram (Equations 15 and 18), the two behaviors are well separated by the line $\Gamma \approx 4\delta/3$ (Figure 9).

Control dykes should not be sensitive to the values of the stress components due to the crater unloading, as they propagate far away from it, while our two coordinates Γ and δ are sensitive to it. With this consideration, the linear relationship $\Gamma \approx 4\delta/3$ separating both regions would thus imply that the behavior of control dykes not only depends on its initial overpressure ΔP_i and the integrated negative buoyancy over the crust thickness $\Delta\rho_c g D_1$, but also on its dimensionless length L^* .

Representing the behavior of each simulation in the space $\Lambda L^* = \Gamma(C\delta)^{-1}$, where C is a constant equal to $\sigma_{rr_{\max}}/\sigma_{rz_{\max}} \approx 8/3$ (see Section 6), as a function of δ (Figure 10a), we now find that those two regions are separated by a horizontal line at $\Lambda L^* \approx 0.5$. This demonstrates that the limit between dykes trapped at depth and dykes reaching the surface is indeed not dependent on the stress component values: ΛL^* does not depend on them and the limit between the two behaviors does not depend on δ , hence nor on $\sigma_{rz_{\max}}$.

Plotting now all dykes behavior in the same parameter spaces (Figures 9b and 10b), we observe that the four different regimes of dyke propagation are also well delineated. A vertical limit at $\delta \approx 0.42 \pm 0.01$ separates two upper regions. On the right of this limit, dykes only reach the surface outside the crater because they are significantly deviated below the crater unloading. On the left of this boundary, dykes are able to reach the surface both within and outside the crater, as they are not efficiently deviated by the crater stress (Figures 9b and 10b). These simulations confirm that the dimensionless number δ controls dyke deviation, as the dykes are completely deviated toward σ_1 for $\delta \gtrsim 0.42 \pm 0.01$. Our value of δ at which dyke deviation is efficient is larger than that proposed by Maccaferri et al. (2019) as we use the maximum value of the shear stress below the unloading (for predictive purposes) while they use the local value of δ resulting from the local shear stress acting on the upper tip of the vertically propagating dyke. The limit between dyke reaching the surface and dyke remaining trapped at depth is also well visible and separated by the horizontal line at $\Lambda L^* = 0.5$ in the diagram ΛL^* as a function of δ (Figure 10b).

The population of particular interest for our study, where the dykes reach the surface only within the crater, is gathered within a small region situated on the left of the vertical limit $\delta \leq 0.42 \pm 0.01$ (pink stars on Figures 9b and 10b). For dykes to reach the surface only within the crater, the deviation due to crater unloading must not be too strong. In both diagrams (Figures 9b and 10b) this category is located along and below the transition boundary highlighted when studying control dykes which separates dyke reaching the surface from those remaining trapped at depth. This behavior is caused by the stress component σ_{rr} which adds up to the magma driving pressure (that scales with ΔP_i) allowing further vertical dyke propagation (Michaut & Pinel, 2018; Michaut et al., 2020), when the deviation is not too important. However, if the radial stress is large enough, the shear stress on vertical dykes is also high and ascending dykes could be considerably deviated from their initial vertical path, which would impede them to reach the surface within the crater.

5. Discussion

5.1. Insights Into the Nature and Thickness of the Crust in the Plateaus

The crustal thickness in the tessera plateaus have been estimated from different types of methods. Before the Magellan mission, Grimm and Solomon (1988) used viscous relaxation of craters to infer a maximum crustal thickness of 10–20 km, whereas Head (1990) found a thickness of 20–30 km in the crustal plateaus from inversions of gravity and topography data. From inversions of Magellan gravity and topography data, Anderson and Smrekar (2006) found that most plateaus have a crustal thickness of 10–30 km, and locally up to 50 km, while Wiczorek (2015) estimated thicknesses between 45 and 65 km, James et al. (2013) between 25 and 45 km and

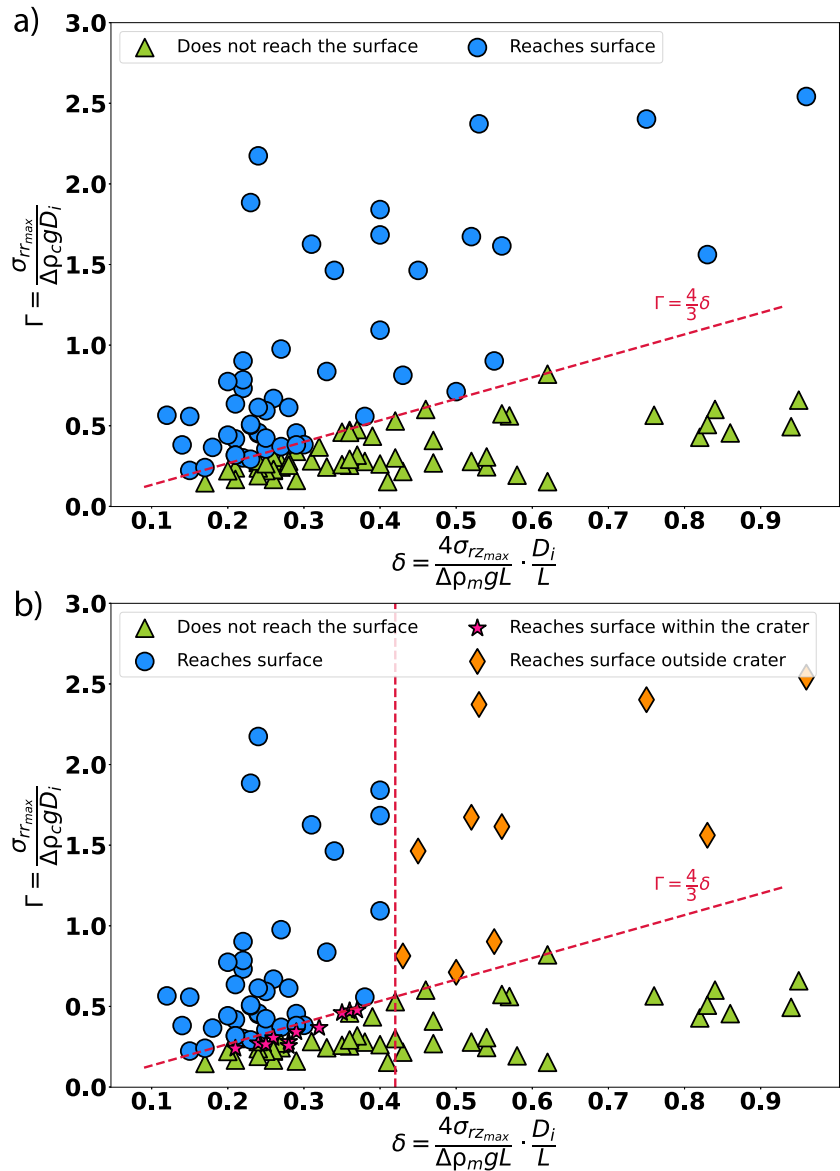


Figure 9. Regime diagram for the 2D propagation of magma dykes in an unloading stress field caused by a crater topography in the parameter space Γ as a function of δ . (a) Behavior for control dykes. Blue dots: control dykes reach the surface, green triangles: control dykes do not reach the surface. (b) Behavior for all dykes. Blue dots: dykes reach the surface everywhere; pink stars: dykes reach the surface only within the crater; orange diamonds: dykes reach the surface only outside the crater; green triangles: dykes remain stored at depth everywhere.

Jiménez-Díaz et al. (2015) from 35 to 55 km. More recently, Maia and Wiczorek (2022) proposed a thickness of 30 km in Ovda Regio and an average value across the crustal plateaus of 25 km. Given that our dark-floored craters are not located on the highest topography areas of these plateaus (Table 2), which are associated to the largest crustal thickness estimates, it is better here to consider average values for the crustal thickness in the plateaus rather than maximum thicknesses.

The population of simulation results we are interested in is the one where dykes reach the surface only within crater (pink stars on Figures 9b and 10b). This population only occurs if dykes are not fully deviated by the crater stress, such that:

$$\delta \lesssim 0.42 \pm 0.01. \quad (19)$$

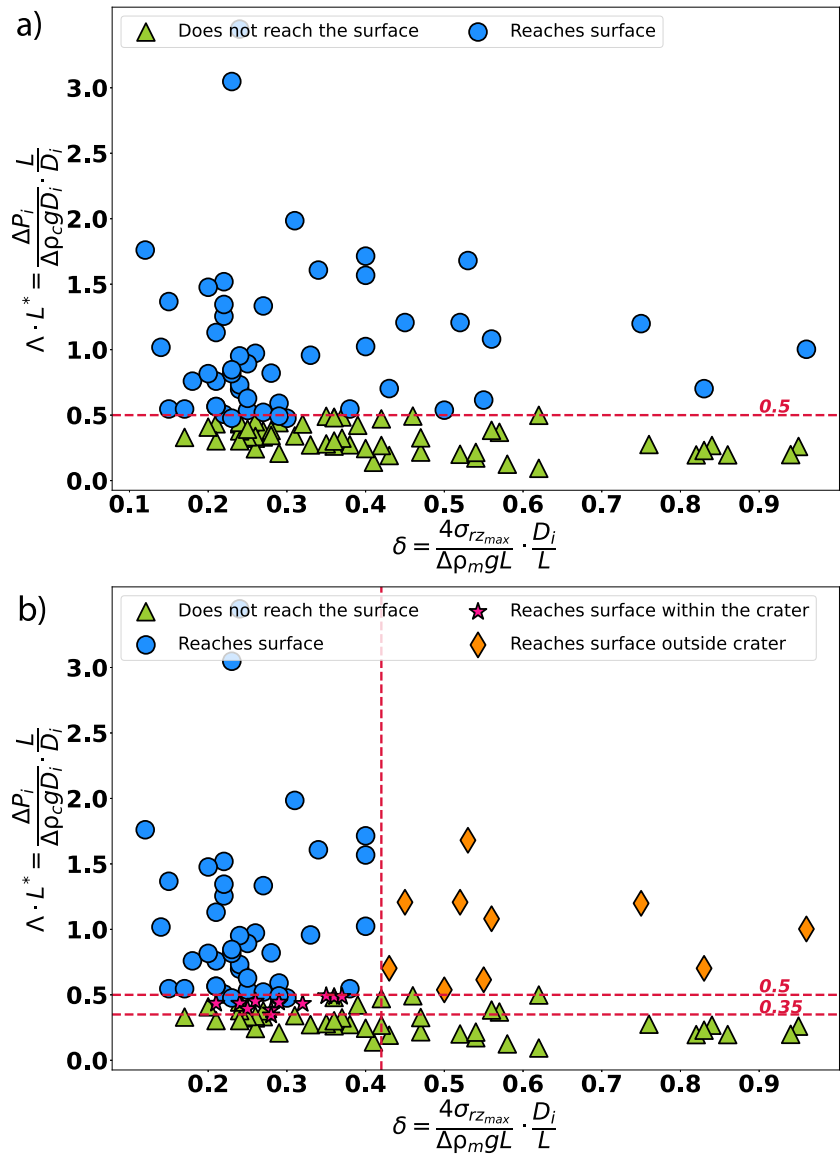


Figure 10. Regime diagram for the 2D propagation of magma dykes in an unloading stress field caused by a crater topography in the parameter space ΛL^* as a function of δ . (a) Behavior for control dykes. Blue dots: control dykes reach the surface, green triangles: control dykes do not reach the surface. (b) Behavior for all dykes. Blue dots: dykes reach the surface everywhere; pink stars: dykes reach the surface only within the crater; orange diamonds: dykes reach the surface only outside the crater; green triangles: dykes remain stored at depth everywhere. Reaching or not the surface for a dyke is controlled by the parameter ΛL^* , while the deviation of the dyke is controlled by the parameter δ . As a consequence, the region of this parameter space for which dykes reach the surface only within the crater is quite narrow ($0.35 < \Lambda L^* < 0.5$ and $\delta < 0.42$).

This helps to constrain the minimum initial dyke length L from Equations 14 and 18:

$$L \gtrsim \left(\frac{4\sigma_{rz_{\max}} D_i}{0.42\Delta\rho_m g} \right)^{1/2} \quad (20)$$

Assuming a small crustal thickness $D_i \geq 10$ km in the plateaus, a value of $\Delta\rho_m = 400 \text{ kg m}^{-3}$ and using a value of $\sigma_{rz_{\max}} = 3.2 \text{ MPa}$ (i.e., an average value for the range of dark-floored crater radii in the plateaus, Figure 6d), we find that L must be larger than 9 km, giving a representative minimum initial overpressure (Equation 14) of $\sim 8 \text{ MPa}$ for the magma. For a crust thickness of 30 km for the Ovda Regio region (Aphrodite Terra), as proposed

by Maia and Wieczorek (2022), we obtain a minimum initial dyke length L of 12 km, and a minimum overpressure of ~ 10 MPa.

On Earth, initial dyke overpressures for non-vesiculated basaltic magma are less than 20 MPa (Bonaccorso et al., 2005). For instance, the initial excess pressure before the dyke propagation was estimated to be 7–15 MPa for the 2001 eruption of Mont Etna (Bonaccorso et al., 2010). Considering a maximum magma overpressure of 15 MPa and a minimum density difference between the mantle and the magma $\Delta\rho_m$ of 400 kg m^{-3} , we obtain a maximum dyke length of 17 km using Equation 14. We thus estimate an initial dyke length in the mantle ranging from 10 to 20 km.

Conversely, Equation 19 now provides the maximum crustal thickness for the magmatic intrusions not to be totally deviated by the unloading:

$$D_i \lesssim \frac{0.42\Delta\rho_m g L^2}{4\sigma_{rz_{\max}}}, \quad (21)$$

which gives $D_i \leq 45$ km for $L \leq 20$ km, in agreement with most crustal thickness estimates from gravity studies (James et al., 2013; Jiménez-Díaz et al., 2015; Maia & Wieczorek, 2022). Hence, eruption of magma only within the crater requires a rather thin crust.

We now constrain the relative density between the crust and magma from Figure 10b. Magma eruption only within the crater requires:

$$0.35 \lesssim \frac{\Delta\rho_m L^2}{4\Delta\rho_c D_i^2} \lesssim 0.50, \quad (22)$$

$$\Leftrightarrow \frac{\Delta\rho_m L^2}{2} \lesssim \Delta\rho_c D_i^2 \lesssim \frac{\Delta\rho_m L^2}{1.4}. \quad (23)$$

From Equations 21 and 23, we deduce:

$$\frac{2\sigma_{rz_{\max}}}{0.42gD_i} \lesssim \Delta\rho_c \lesssim \frac{\Delta\rho_m L^2}{1.4D_i^2}. \quad (24)$$

For D_i between 20 and 45 km, $L \leq 20$ km, $\Delta\rho_m = 400 \text{ kg m}^{-3}$, $\sigma_{rz_{\max}} \approx 3.2 \text{ MPa}$, Equation 24 constraints the density contrast between the magma and the crust to be between 37 and 285 kg m^{-3} . Both the minimum and maximum values of $\Delta\rho_c$ decrease as the crustal thickness D_i increases (Equation 24, Figure 11). For the average crustal thickness of 30 km estimated in the Ovda region (Maia & Wieczorek, 2022), we obtain a density contrast between 57 and 127 kg m^{-3} for magma eruption on the crater floor only.

Discussion about the composition of the crustal plateaus have been ongoing since the VIRTIS emissivity data hinted at a possible felsic composition (Gilmore et al., 2015, 2017; Hashimoto et al., 2008; Mueller et al., 2008), in particular in Alpha Regio. However, these emissivity data could also correspond to weathered basaltic rocks or to a low ferrous iron content of the crustal rocks (Gilmore et al., 2017). Our results suggest that the crustal plateaus might indeed be slightly differentiated, although this differentiation appears limited given available estimates of the crustal thicknesses in those areas. This is in line with the study of Nimmo and Mackwell (2023), which demonstrates that a quartz-dominated rheology cannot explain the longevity and survival of crustal plateaus. A better resolution of the crustal thickness at the location of the dark-floored craters would help refine our constraints. These constraints might be brought in the near future by the upcoming NASA and ESA missions to Venus and their gravity and topography measurements. In particular, the smaller the crustal thickness, the larger the maximum density contrast between the magma and crust can be for magma eruption only in the crater interior (Figure 11).

5.2. Volcanic Plains Versus Crustal Plateaus

In contrast with the crustal plateaus, the plains of Venus are covered by lava (Basilevsky & Head, 2003). One possibility is that magma is buoyant in the crust forming the plains (i.e., $\rho_c > \rho_{\text{mag}}$). Another possibility is that

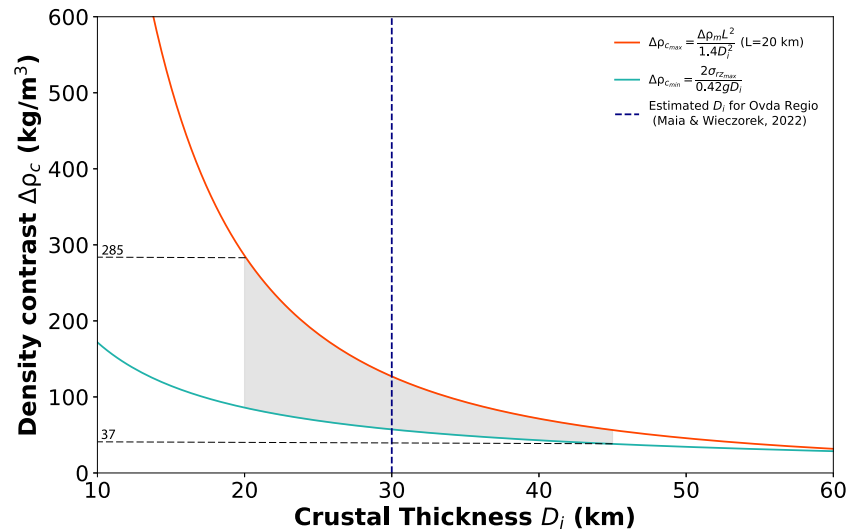


Figure 11. Density contrast between magma and crust $\Delta\rho_c$ as a function of crustal thickness D_i as constrained by Equation 24. The maximum value is calculated for the maximum dyke length $L = 20$ km. The gray area corresponds to the admissible range for the average crustal thickness in the plateaus, and the vertical blue dashed line represents the estimated crust thickness in Onda Regio in Aphrodite Terra (Maia & Wiczcerek, 2022). We use $\sigma_{rz,max} = 3.2$ MPa the average of the maximum shear stress considered in this study.

$\rho_c < \rho_{mag}$ and the volcanic regime in the plains then corresponds to the region of the blue dots on Figures 9 and 10. In that case, we can use the results of our simulations to get some insights into the properties of the crust in the plains regions. As dark-floored craters with complete ejecta blankets can be observed in the plains (e.g., Bassi in Herrick's database), this suggests that craters can be filled by lavas from the interior and hence that dyke deviation due to the crater topography is not sufficient to preclude eruption on the crater floor, which requires $\delta < 0.42 \pm 0.01$. This again constrains the minimum initial dyke length from Equation 20. Assuming a small crustal thickness $D_i \geq 10$ km in the plains, a value of $\Delta\rho_m = 400 \text{ kg m}^{-3}$ and using again $\sigma_{rz,max} = 3.2$ MPa that is appropriate for a large range of crater radius (Figure 6d), we find that L must be larger than 9 km, giving a minimum initial overpressure (Equation 14) of 8 MPa for the magma. Moreover, comparing the rim-floor depth of dark-floored craters relatively to bright-floored craters in the plateaus and in the plains, we note that dark-floored craters in the plains are shallower than in the plateaus (see Figure 4c that compares our power law for Δh in the plateaus with the one obtained by Herrick and Rumpf (2011) for the plains). Although our error bars are quite large, the thickness of the magmatic infilling seems higher in the plains by about 30%, suggesting that magma eruption and crater filling by lava is easier in the plains, as expected, either because the crust is thinner or denser. If dark-floored craters are filled by the same material that makes up the plains, as suggested from radar observations (Phillips et al., 1992), and given that the material constituting the plains is likely of basaltic composition (Basilevsky & Head, 2003), our results suggest that the crust forming the plateaus of Venus could be thicker or slightly less dense than in the plains (when comparing blue dots and pink stars in Figure 10b). The latter could arise from a moderately more felsic composition of the crust in the plateaus or from a difference in porosity resulting from magma degassing being more important in the plateaus because of the lower surface pressure (Head & Wilson, 1992).

5.3. Bright-Floored, Dark-Floored, and Floor-Fractured Craters

While we interpret dark-floored craters in the plateaus as craters being modified after their formation by eruption and filling by lava from the crater interior, and constrain the underlying crust properties from our regime diagram (Figure 9), we cannot conclude as regards to the bright-floored craters. Although it would be tempting to interpret them as craters that cannot be filled because their radius is too large, causing a large shear stress $\sigma_{rz,max}$ and storage below the unloading (i.e., $\delta \geq 0.42$, Figure 9), there does not seem to exist significant size differences between dark and bright-floored craters in the plateaus (Figure 5), and the resolution of the crustal thickness map is not yet good enough to investigate the influence of lateral variations in crustal thickness as done on the Moon (Michaut & Pinel, 2018; Walwer et al., 2021). On another hand, Campbell et al. (1992) showed that dark parabolic deposits,

resulting from extended ejecta deposits, are associated to bright-floored craters, allowing to interpret them as young. The fact that few to no dark-floored craters have dark parabolic deposits therefore leads to believe they are older structures, modified by volcanism. This suggests in turn that bright-floored craters in the plateaus could have the potential of becoming dark-floored. Our model is not able to provide constraints on the time scale needed for the crater to be modified by volcanism, although, on timescales larger than millions of years, viscous relaxation may relax at least part of the elastic stresses caused by the crater topography. Viscous relaxation effects may also be considered by introducing an “effective crater stress field,” simply obtained by reducing the elastic stress by a certain fraction (Maccaferri et al., 2017). However in the current application to Venus, the percent of viscous stress relaxation might only be introduced as a free parameter, as we do not have constraints for it. We can thus consider our elastic stress calculation as an upper-edge estimate of the actual stress acting within the lower crust of Venus. In the case of a partially relaxed topography, we would expect the non-diagonal stress component of the stress field to be smaller, which would result in a larger possible crustal thickness below the plateaus. Finally, lateral variation in melt productivity, caused by variations in heat flow, may also exist, and could affect the initial amount of magma available for ascent and crater floor modification and explain the difference between the two populations of craters.

Observations show that dark-floored craters occur on Venus over a wide range of elevations and crustal thicknesses. Magma being able to reach the interior of the crater on Venus indicates little deviation of the ascending dyke ($\delta < 0.42$), both in the plains, where the crust is supposedly thin, and in the plateaus, where the crust is probably thicker and deviation easier. The formation of floor-fractured craters requires, on the contrary, a significant deviation of the ascending dykes to form shallow, crater-centered, sill-like intrusions (Jozwiak et al., 2012; Schultz, 1976; Thorey & Michaut, 2014). Thus, conditions on Venus do not favor magma deviation below craters and the formation of floor-fractured craters. In fact, only three floor-fractured craters have been recognized on Venus, two of them being currently registered in the official crater databases (Barrymore and Mona Lisa). These craters are located at low elevations, in the plains (Wichman & Schultz, 1995) and are identified as dark-floored craters. By analogy with some lunar floor-fractured craters located in the Maria, we suggest that these fractures could form by inflation of previously erupted and solidified lavas during subsequent episodes of magma eruption (Walwer et al., 2021).

6. Conclusion

Dark-floored craters on Venus are considered to be partially filled by magmatic material and are shallower than their bright-floored counterparts. On the crustal plateaus, they can easily be identified as they contrast with the radar-bright, highly deformed terrain where they are located. As their ejecta blankets and rims show no clear sign of crosscutting on SAR images, it is likely that these craters are not embayed by an external source, suggesting their infilling could be linked to the crater itself. We use numerical simulations of dyke propagation in an external stress field caused by the crater topography to draw a regime diagram showing the different possible behaviors of a dyke ascending below a crater. We identify four possible behaviors (magma storage, magma eruption on the crater floor only, magma eruption outside of the crater only or magma eruption everywhere), including one where the magma only reaches the surface within the crater. Our numerical simulations suggest that situations where the magma reaches only the crater floor, as observed in the plateaus of Venus, requires a crust thinner than 45 km and a negative magma buoyancy in the crust with a rather small magma-crust density contrast between 37 and 285 kg m⁻³ for crustal thicknesses between 20 and 45 km. Upcoming NASA and ESA missions to Venus VERITAS (S. Smrekar et al., 2022) and ENVISION (Rosenblatt et al., 2021) will provide higher resolution topographic maps of the surface as well as gravity measurements that will allow for a more precise estimation of the magmatic filling thickness within the craters as well as new insights on Venus internal structure, including crustal thickness maps from gravitational studies, which will further constrain our density contrast estimates.

Data Availability Statement

The code for dyke propagation in an external stress field is available in a Zenodo repository (Maccaferri, 2020). The semi_infinite_stress_field.m MatLab code used to compute the crater stress field in a semi-infinite half-space in axisymmetric geometry is also provided in a Zenodo repository (Le Contellec, 2024a). Simulation results of dyke propagation in the crater stress field can be found in a repository (Le Contellec, 2024b). The crater database

used in this study was developed by R. Herrick and can be found at <https://www.lpi.usra.edu/resources/vc/vchome.html>.

Acknowledgments

This project has received funding from the European Research Council (ERC) under the European Union's Horizon 2020 research and innovation program (grant agreement no. 101001689). The authors would like to thank the Editor and Associated Editor as well as Taras Gerya and Zhongfan Liu for their comments that helped improve this manuscript.

References

- Anderson, F., & Smrekar, S. (2006). Global mapping of crustal and lithospheric thickness on Venus. *Journal of Geophysical Research*, *111*(E8), 1517–1520. <https://doi.org/10.1029/2004JE002395>
- Aoki, Y., Segall, P., Kato, T., Cervelli, P., & Shimada, S. (1999). Imaging magma transport during the 1997 seismic swarm off the Izu Peninsula, Japan. *Science*, *286*(5441), 927–930. <https://doi.org/10.1126/science.286.5441.927>
- Barsukov, V., Basilevsky, A., Burba, G., Bobinna, N., Kryuchkov, V., Kuzmin, R., et al. (1986). The geology and geomorphology of the Venus surface as revealed by the radar images obtained by Venera 15 and 16. *Journal of Geophysical Research*, *91*(B4), 378–398. <https://doi.org/10.1029/JB091iB04p0D378>
- Basilevsky, A. T., & Head, J. W. (1998). The geologic history of Venus: A stratigraphic view. *Journal of Geophysical Research*, *103*(E4), 8531–8544. <https://doi.org/10.1029/98JE00487>
- Basilevsky, A. T., & Head, J. W. (2003). The surface of Venus. *Reports on Progress in Physics*, *66*(10), 1699–1734. <https://doi.org/10.1088/0034-4885/66/10/R04>
- Basilevsky, A. T., Ivanov, B., Burra, G., Chernaaya, L., Kryuchkov, V., Nikolaeva, O., et al. (1987). Impact craters of Venus: A continuation of the analysis of data from the Venera 15 and 16 spacecraft. *Journal of Geophysical Research*, *91*(B12), 12869–12901. <https://doi.org/10.1029/JB092iB12p12869>
- Basilevsky, A. T., Ivanov, M., Head, J. W., Aittola, M., & Raitala, J. (2007). Landing on Venus: Past and future. *Planetary and Space Science*, *55*(14), 2097–2112. <https://doi.org/10.1016/j.pss.2007.09.005>
- Basilevsky, A. T., Pronin, A. A., Ronca, L., Kryuchkov, V., Sukhanov, A., & Markov, M. (1986). Styles of tectonic deformations on Venus: Analysis of Venera 15 and 16 data. *Journal of Geophysical Research*, *91*(B4), 399–411. <https://doi.org/10.1029/JB091iB04p0D399>
- Battaglia, J., Ferrazzini, V., Staudacher, T., Aki, K., & Cheminée, J.-L. (2005). Pre-eruptive migration of earthquakes at the Piton de la Fournaise volcano (Réunion Island). *Geophysical Journal International*, *161*(2), 549–558. <https://doi.org/10.1111/j.1365-246X.2005.02606.x>
- Beauducel, F., Peltier, A., Villié, A., & Suryanto, W. (1999). Mechanical imaging of a volcano plumbing system from GNSS unsupervised modeling. *Geophysical Research Letters*, *47*(17), e2020GL089419. <https://doi.org/10.1029/2020GL089419>
- Bindschadler, D. L., Schaber, G. G., & Williams, M. K. (1992). Coldspots and hotspots: Global tectonics and mantle dynamics of Venus. *Journal of Geophysical Research*, *97*(E8), 13495–13532. <https://doi.org/10.1029/92JE01165>
- Bonaccorso, A., Cianetti, S., Giunchi, C., Transatti, E., Bonafede, M., & Boschi, E. (2005). Analytical and 3-D numerical modelling of Mt. Etna (Italy) volcano inflation. *Geophysical Journal International*, *163*(2), 852–862. <https://doi.org/10.1111/j.1365-246X.2005.02777.x>
- Bonaccorso, A., Currenti, G., Negro, C. D., & Boschi, E. (2010). Dike deflection modelling for inferring magma pressure and withdrawal, with application to Etna 2001 case. *Earth and Planetary Science Letters*, *293*(1–2), 121–129. <https://doi.org/10.1016/j.epsl.2010.02.030>
- Campbell, D., Stacy, N., Newman, W., Arvidson, R., Jones, E., Musser, G., et al. (1992). Magellan observations of extended impact crater related features on the surface of Venus. *Journal of Geophysical Research*, *97*(E10), 16249–16277. <https://doi.org/10.1029/92JE01634>
- Christensen, P., Engle, E., Anwar, S., Dickensfield, S., Noss, D., Gorelick, N., & Weiss-Malik, M. (2009). *JMARS—A planetary GIS*. American Geophysical Union, Fall Meeting. Retrieved from <http://adsabs.harvard.edu/abs/2009AGUFMIN22A..06C>
- Corbi, F., Rivalta, E., Pinel, V., Maccaferri, F., & Acocella, V. (2016). Understanding the link between circumferential dikes and eruptive fissures around calderas based on numerical and analog models. *Geophysical Research Letters*, *43*(12), 6212–6219. <https://doi.org/10.1002/2016GL068721>
- Cotterell, B., & Rice, J. (1980). Slightly curved or kinked cracks. *International Journal of Fracture*, *16*(2), 155–169. <https://doi.org/10.1007/BF00012619>
- Dahm, T. (2000). Numerical simulations of the propagation path and the arrest of fluid-filled fractures in the Earth. *Geophysical Journal International*, *141*(3), 623–638. <https://doi.org/10.1046/j.1365-246x.2000.00102.x>
- Ernst, R., Head, J., Parfitt, E., Grosfils, E., & Wilson, L. (1995). Giant radiating dyke swarms on Earth and Venus. *Earth-Science Reviews*, *39*(1–2), 1–58. [https://doi.org/10.1016/0012-8252\(95\)00017-5](https://doi.org/10.1016/0012-8252(95)00017-5)
- Ford, P. G., & Pettengill, G. H. (1992). Venus topography and kilometer-scale slopes. *Journal of Geophysical Research*, *97*(E8), 13103–13114. <https://doi.org/10.1029/92JE01085>
- Gerya, T. V. (2014). Plume-induced crustal convection: 3D thermomechanical model and implications for the origin of novae and coronae on Venus. *Earth and Planetary Science Letters*, *391*(1), 183–192. <https://doi.org/10.1016/j.epsl.2014.02.005>
- Ghent, R., & Hansen, V. (1998). Structural and kinematic analysis of eastern Ovda Regio, Venus: Implications for crustal plateau formation. *Icarus*, *139*(1), 116–136. <https://doi.org/10.1006/icar.1999.6085>
- Gilmore, M. S., Collins, G. C., Ivanov, M. A., Marinangeli, L., & Head, J. W. (1994). Style and sequence of extensional structures in tessera terrain, Venus. *Geophysical Research Letters*, *21*(8), 701–704.
- Gilmore, M. S., & Head, J. W. (2000). Sequential deformation of plains at the margins of Alpha Regio, Venus: Implications for tessera formation. *Meteoritics & Planetary Sciences*, *35*(4), 667–687. <https://doi.org/10.1111/j.1945-5100.2000.tb01451.x>
- Gilmore, M. S., Mueller, N., & Helbert, J. (2015). VIRTIS emissivity of Alpha Regio, Venus, with implications for tessera composition. *Icarus*, *254*(1), 350–361. <https://doi.org/10.1016/j.icarus.2015.04.008>
- Gilmore, M. S., Treiman, A., Helbert, J., & Smrekar, S. (2017). Venus surface composition constrained by observation and experiment. *Space Science Reviews*, *11*(1963), 1511–1540. <https://doi.org/10.1007/s11214-017-0370-8>
- Grieve, R. A., & Cintala, M. (1995). Impact melting on Venus: Some considerations for the nature of the cratering record. *Icarus*, *114*(1), 68–79. <https://doi.org/10.1006/icar.1995.1044>
- Grimm, R. E., & Solomon, S. C. (1988). Viscous relaxation of impact relief on Venus: Constraints on crustal thickness and thermal gradient. *Journal of Geophysical Research*, *93*(B10), 11911–11929. <https://doi.org/10.1029/JB093iB10p11911>
- Grosfils, E. B., & Head, J. W. (1994). The global distribution of giant radiating dike swarms on Venus: Implications for the global stress state. *Geophysical Research Letters*, *21*(8), 701–704. <https://doi.org/10.1029/94GL00592>
- Hansen, V. L. (2006). Geologic constraints on crustal plateau surface histories, Venus: The lava pond and bolide impact hypotheses. *Journal of Geophysical Research*, *111*(E11), E11010. <https://doi.org/10.1029/2006JE002714>
- Hansen, V. L., Phillips, R., & Ghent, R. R. (2000). Structures in tessera terrain, Venus: Issues and answers. *Journal of Geophysical Research*, *105*(E2), 4135–4152. <https://doi.org/10.1029/1999JE001137>

- Hashimoto, G. L., Serote, M. R., Sugita, S., Gilmore, M., Kamp, L. W., Carlson, R. W., & Baines, K. H. (2008). Felsic Highlands crust on Venus suggested by Galileo near-infrared mapping spectrometer data. *Journal of Geophysical Research*, *113*(E5), E00B24. <https://doi.org/10.1029/2008JE003134>
- Hauck, S. A., Phillips, R., & Price, M. H. (1998). Venus crater distribution and plains resurfacing models. *Journal of Geophysical Research*, *103*(E6), 13635–13642. <https://doi.org/10.1029/98JE00400>
- Head, J. W. (1990). Processes of crustal formation and evolution on Venus: An analysis of topography, hypsometry and crustal variation. *Earth, Moon, and Planets*, *50*(1), 20–55. <https://doi.org/10.1007/BF00142388>
- Head, J. W., & Wilson, L. (1992). Magma reservoirs and neutral buoyancy zones on Venus: Implications for the formation and evolution of volcanic landforms. *Journal of Geophysical Research*, *97*(E3), 3877–3903. <https://doi.org/10.1029/92JE00053>
- Head, J. W., & Wilson, L. (1998). Magmatic intrusion-related processes in the upper lunar crust: The role of country rock porosity/permeability in magmatic percolation and thermal annealing, and implications for gravity signatures. *Journal of Geophysical Research*, *103*(E7), 16813–16840. <https://doi.org/10.1029/98JE01322>
- Helbert, J., Müller, N., Kostama, P., Marinangeli, L., Piccioni, G., & Drossart, P. (2008). Surface brightness variations seen by VIRTIS on Venus Express and implications for the evolution of the Lada Terra region, Venus. *Geophysical Research Letters*, *35*, L11201. <https://doi.org/10.1029/2008GL033609>
- Herrick, R. R., & Phillips, R. (1994). Implications of a global survey of Venusian impact craters. *Icarus*, *111*(2), 387–416. <https://doi.org/10.1006/icar.1994.1152>
- Herrick, R. R., & Rumpf, M. E. (2011). Postimpact modification by volcanic or tectonic processes as the rule, not the exception, for Venusian craters. *Journal of Geophysical Research*, *116*(E2), E02004. <https://doi.org/10.1029/2010JE003722>
- Herrick, R. R., & Sharpton, V. L. (2000). Implications from stereo-derived topography of Venusian craters. *Journal of Geophysical Research*, *105*(E8), 20245–20262. <https://doi.org/10.1029/1999JE001225>
- Herrick, R. R., Sharpton, V. L., Malin, M. C., Lyons, S. N., & Feely, K. (1997). *Morphology and morphometry of impact craters (Venus II)*. University of Arizona Press.
- Herrick, R. R., Stahlke, D. L., & Sharpton, V. L. (2012). Fine-scale Venusian topography from Magellan stereo data. *EOS*, *93*(12), 125–126. <https://doi.org/10.1029/2012EO120002>
- Ivanov, B. (1990). Venusian impact craters on Magellan images: View from Venera 15/16. *Earth, Moon, and Planets*, *50*(1), 159–173. <https://doi.org/10.1007/BF00142393>
- Ivanov, B., & Melosh, H. (1995). Impacts do not initiate volcanic eruptions: Eruptions close to the crater. *Geology*, *31*(10), 869–872. <https://doi.org/10.1130/G19669.1>
- Ivanov, M., & Basilevsky, A. T. (1993). Density and morphology of impact craters on tessera terrain, venus. *Geophysical Research Letters*, *20*(23), 2579–2582. <https://doi.org/10.1029/93GL02692>
- Ivanov, M., & Head, J. W. (1996). Tessera terrain on venus: A survey of the global distribution, characteristics and relation to surrounding units from Magellan data. *Journal of Geophysical Research*, *101*(E6), 14861–14908. <https://doi.org/10.1029/96JE01245>
- Ivanov, M., & Head, J. W. (2011). Global geological map of Venus. *Planetary and Space Science*, *59*(13), 1559–1600. <https://doi.org/10.1016/j.pss.2011.07.008>
- Izenberg, N., Arvidson, R. E., & Phillips, R. (1994). Impact crater degradation on Venusian plains. *Geophysical Research Letters*, *21*(4), 284–292. <https://doi.org/10.1029/94GL00080>
- James, P. B., Zuber, M. T., & Phillips, R. (2013). Crustal thickness and support topography of Venus. *Journal of Geophysical Research: Planets*, *118*(4), 859–875. <https://doi.org/10.1029/2012JE004237>
- Jiménez-Díaz, A., Ruiz, J., Kirby, J., Romeo, I., Tejero, R., & Capote, R. (2015). Lithospheric structure of Venus from gravity and topography. *Icarus*, *260*(1), 215–231. <https://doi.org/10.1016/j.icarus.2015.07.020>
- Jozwiak, L. M., Head, J. W., Zuber, M. T., Smith, D. E., & Neumann, G. A. (2012). Lunar floor-fractured craters: Classification, distribution, origin and implications for magmatism and shallow crustal structure. *Journal of Geophysical Research*, *117*(E11), E11005. <https://doi.org/10.1029/2012JE004134>
- Kargel, J., Komatsu, G., & Strom, R. G. (1993). The volcanology of Venera and VEGA landing sites and the geochemistry of Venus. *Icarus*, *103*(2), 253–275. <https://doi.org/10.1006/icar.1993.1069>
- Le Contellec, A. (2024a). Computing the stress field resulting from a surface topographic load on top of a semi-infinite elastic medium in axisymmetric geometry. *Zenodo*. <https://doi.org/10.5281/zenodo.8348775>
- Le Contellec, A. (2024b). Supporting information for “insights into venus’ crustal plateaus from dyke trajectories below craters” (simulation results). *Zenodo*. <https://doi.org/10.5281/zenodo.10666555>
- Lister, J. R. (1990). Buoyancy-driven fluid fracture: Similarity solutions for the horizontal and vertical propagation of fluid-filled cracks. *Journal of Fluid Mechanics*, *217*, 213–239. <https://doi.org/10.1017/S0022112090000696>
- Lister, J. R. (1991). Steady solutions for feeder dykes in a density-stratified lithosphere. *Earth and Planetary Science Letters*, *107*(2), 233–242. [https://doi.org/10.1016/0012-821X\(91\)90073-Q](https://doi.org/10.1016/0012-821X(91)90073-Q)
- Maccaferri, F. (2020). Dyke propagation code for: The rebirth and evolution of Bezmyianny volcano after the 1956 sector collapse. *Zenodo*. <https://doi.org/10.5281/zenodo.3957577>
- Maccaferri, F., Bonafede, M., & Rivalta, E. (2010). A numerical model of dyke propagation in layered elastic medium. *Geophysical Journal International*, *180*(3), 1107–1123. <https://doi.org/10.1111/j.1365-246X.2009.04495.x>
- Maccaferri, F., Bonafede, M., & Rivalta, E. (2011). A quantitative study of the mechanisms governing dike propagation, dike arrest and sill formation. *Journal of Volcanology and Geothermal Research*, *208*(1–2), 39–50. <https://doi.org/10.1016/j.jvolgeores.2011.09.001>
- Maccaferri, F., Richter, N., & Walter, T. R. (2017). The effect of giant lateral collapses on magma pathways and the location of volcanism. *Nature*, *8*(1097), 1097. <https://doi.org/10.1038/s41467-017-01256-2>
- Maccaferri, F., Rivalta, E., Keir, D., & Acocella, V. (2014). Off-rift volcanism in rift zones determined by crustal unloading. *Nature Geoscience*, *7*(4), 297–300. <https://doi.org/10.1038/NGEO2110>
- Maccaferri, F., Smittarello, D., Pinel, V., & Cayol, V. (2019). On the propagation path of magma-filled dikes and hydrofractures: The competition between external stress, internal pressure and crack length. *Geochemistry, Geophysics, Geosystems*, *20*(4), 2064–2081. <https://doi.org/10.1029/2018GC007915>
- Maia, J. S., & Wiczorek, M. A. (2022). Lithospheric structure of Venusian crustal plateaus. *Journal of Geophysical Research: Planets*, *127*(2), e2021JE007004. <https://doi.org/10.1029/2021JE007004>
- Manske, L., Marchi, S., Plesa, A.-C., & Wunemann, K. (2021). Impact melting upon basin formation on early Mars. *Icarus*, *357*(15), 114128. <https://doi.org/10.1016/j.icarus.2020.114128>

- Michaut, C., & Pinel, V. (2018). Magma ascent and eruption triggered by cratering on the Moon. *Geophysical Research Letters*, 45(13), 6408–6416. <https://doi.org/10.1029/2018GL078150>
- Michaut, C., Pinel, V., & Maccaferri, F. (2020). Magma ascent at floor-fractured craters diagnoses the lithospheric stress state on the Moon. *Earth and Planetary Science Letters*, 530(530), 115889. <https://doi.org/10.1016/j.epsl.2019.115889>
- Mueller, N., Helbert, J., Hashimoto, G., Tsang, C., Erard, S., Piccioni, G., & Drossart, P. (2008). Venus surface thermal emission at 1 μm in VIRTIS imaging observations: Evidence for variation of crust and mantle differentiation conditions. *Journal of Geophysical Research*, 113, E00B17. <https://doi.org/10.1029/2008JE003118>
- Nimmo, F., & Mackwell, S. (2023). Viscous relaxation as a probe of heat flux and crustal plateau composition on Venus. *PNAS: Earth, Atmospheric and Planetary Sciences*, 120(3), e2216311120. <https://doi.org/10.1073/pnas.2216311120>
- Peltier, A., Ferrazzini, V., Staudacher, T., & Bachèlery, P. (2005). Imaging the dynamics of dyke propagation prior to the 2000–2003 flank eruptions at Piton de La Fournaise, Reunion Island. *Geophysical Research Letters*, 32, L22302. <https://doi.org/10.1029/2005GL023720>
- Peltier, A., Staudacher, T., & Bachèlery, P. (2007). Constraints on magma transfers and structures involved in the 2003 activity at Piton de La Fournaise from displacement data. *Geophysical Research Letters*, 112, B03207. <https://doi.org/10.1029/2006JB004379>
- Phillips, R., Grimm, R. E., & Malin, M. C. (1991). Hot-spot evolution and the global tectonics of Venus. *Science*, 252(5006), 651–658. <https://doi.org/10.1126/science.252.5006.651>
- Phillips, R., & Hansen, V. L. (1994). Tectonic and magmatic evolution of Venus. *Annual Review of Earth and Planetary Sciences*, 22(1), 597–654. <https://doi.org/10.1146/annurev.earth.22.050194.003121>
- Phillips, R., Raubertas, R. F., Arvidson, R. E., Sarkar, I. C., Herrick, R. R., Izenberg, N., & Grimm, R. E. (1992). Impact craters and Venus resurfacing history. *Journal of Geophysical Research*, 97(E10), 15923–15948. <https://doi.org/10.1029/92JE01696>
- Pinel, V., Carrara, A., Maccaferri, F., Rivalta, E., & Corbi, F. (2017). A two-step model for dynamical dike propagation in two dimensions: Application to the July 2001 Etna eruption. *Journal of Geophysical Research: Solid Earth*, 122(2), 1107–1125. <https://doi.org/10.1002/2016JB013630>
- Rivalta, E., Taisne, B., Bungler, A., & Katz, R. (2015). A review of mechanical models of dike propagation: Schools of thought, results and future directions. *Tectonophysics*, 638, 1–42. <https://doi.org/10.1016/j.tecto.2014.10.003>
- Romeo, I., & Capote, R. (2011). Tectonic evolution of Ovda Regio: An example of highly deformed continental crust on Venus? *Planetary and Space Science*, 59(13), 1428–1445. <https://doi.org/10.1016/j.pss.2011.05.013>
- Romeo, I., & Turcotte, D. (2010). Resurfacing of Venus. *Planetary and Space Science*, 58(10), 1374–1380. <https://doi.org/10.1016/j.pss.2010.05.022>
- Rosenblatt, P., Dumoulin, C., Marty, J.-C., & Genova, A. (2021). Determination of Venus' interior structure with EnVision. *Remote Sensing*, 13(9), 1624. <https://doi.org/10.3390/rs13091624>
- Schaber, G., Strom, R., Moore, H., Soderblom, L., Kirk, R., Chadwick, D., et al. (1992). Geology and distribution of impact craters on Venus: What are they telling us? *Journal of Geophysical Research*, 97(E8), 13257–13301. <https://doi.org/10.1029/92JE01246>
- Schultz, P. H. (1976). Floor-fractured lunar craters. *The Moon*, 15(3), 241–273. <https://doi.org/10.1007/BF00562240>
- Schultz, P. H. (1978). Martian intrusions: Possible sites and implications. *Geophysical Research Letters*, 5(6), 457–460. <https://doi.org/10.1029/GL005i006p00457>
- Sharpton, V. L. (1994). Evidence from Magellan for unexpectedly deep complex craters on Venus. *Geological Society of America Special Paper, Large Meteorite Impacts and Planetary Evolution*, 19–28. <https://doi.org/10.1130/SPE293-p19>
- Smrekar, S., Hensley, S., Nybakken, R., Wallace, M. S., Perkovic-Martin, D., You, T.-H., et al. (2022). VERITAS (venus emissivity, radio science, InSAR, topography, and spectroscopy): A discovery mission. In *2022 IEEE aerospace conference (AERO)* (pp. 1–20). <https://doi.org/10.1109/AEROS3065.2022.9843269>
- Smrekar, S. E., & Phillips, R. (1991). Venusian Highlands: Geoid to topography ratios and their implications. *Earth and Planetary Science Letters*, 107(3–4), 582–597. [https://doi.org/10.1016/0012-821X\(91\)90103-0](https://doi.org/10.1016/0012-821X(91)90103-0)
- Sneddon, I. N. (1951). *Fourier transforms*. McGraw-Hill Book Company.
- Stofan, E. R., & Smrekar, S. E. (2005). Large topographic rises, coronae, large flow fields, and large volcanoes on Venus: Evidence for mantle plumes? *Geological Society of America Special Paper*, 388, 841–861. <https://doi.org/10.1130/0-8137-2388-4.841>
- Strom, R. G., Schaber, G., & Dawson, D. (1994). The global resurfacing of Venus. *Journal of Geophysical Research*, 99(E5), 10899–10926. <https://doi.org/10.1029/94JE00388>
- Surkov, Y. A., Barsukov, V. L., Moskal'yeva, L. P., Kharyukova, V. P., & Kemurdzian, A. L. (1984). New data on the composition, structure, and properties of Venus rock obtained by Venera 13 and Venera 14. *Journal of Geophysical Research*, 89(S02), B393–B402. <https://doi.org/10.1029/JB089iS02p0B393>
- Surkov, Y. A., Moskal'yeva, L. P., Shcheglov, O. P., Kharyukova, V. P., Manvelyan, O. S., Kirichenko, V. S., & Dudin, A. D. (1983). Determination of the elemental composition of rocks on Venus by Venera 13 and Venera 14 (preliminary results). *Journal of Geophysical Research*, 88(S02), A481–A493. <https://doi.org/10.1029/JB088iS02p0A481>
- Surkov, Y. A., Moskal'yova, L. P., Kharyukova, V. P., Dudin, A. D., Smirnov, G. G., & Zaitseva, S. Y. (1986). Venus rock composition at the Vega 2 landing site. *Journal of Geophysical Research*, 91(B13), E215–E218. <https://doi.org/10.1029/JB091iB13p0E215>
- Thorey, C., & Michaut, C. (2014). A model for the dynamics of crater-centered intrusion: Application to lunar floor-fractured craters. *Journal of Geophysical Research: Planets*, 119(1), 286–312. <https://doi.org/10.1002/2013JE004467>
- Thorey, C., Michaut, C., & Wieczorek, M. (2015). Gravitational signatures of Lunar floor-fractured craters. *Earth and Planetary Science Letters*, 424(1), 269–279. <https://doi.org/10.1016/j.epsl.2015.04.021>
- Walwer, D., Michaut, C., Pinel, V., & Adda-Bedia, M. (2021). Magma ascent and emplacement below floor-fractured craters on the Moon from floor uplift and fracture length. *Physics of the Earth and Planetary Interiors*, 312(1), 106658. <https://doi.org/10.1016/j.pepi.2021.106658>
- Watanabe, T., Masuyama, T., Nagaoka, K., & Tahara, T. (2002). Analog experiments on magma-filled cracks: Competition between external stresses and internal pressure. *Earth Planets and Space*, 54(1), e1247–e1261. <https://doi.org/10.1186/BF03352453>
- Weertman, J. (1971). Theory of water-filled crevasses in glaciers applied to vertical magma transport beneath ocean ridges. *Journal of Geophysical Research*, 76(5), 1171–1183. <https://doi.org/10.1029/JB076i005p01171>
- Wichman, R. W. (1999). Internal crater modification on Venus: Recognizing crater-centered volcanism by changes in floor morphometry and floor brightness. *Journal of Geophysical Research*, 104(E9), 21957–21977. <https://doi.org/10.1029/1997JE000428>
- Wichman, R. W., & Schultz, P. H. (1995). Floor-Fractured craters on Mars—observations and origins. *Journal of Geophysical Research: Planets*, 100(E2), 3233–3244. <https://doi.org/10.1029/94JE03206>
- Wieczorek, M. (2015). Gravity and topography of the terrestrial planets. *Treatise on Geophysics*, 10(1), 165–206. <https://doi.org/10.1016/B978-0-444-53802-4.00169-X>

Wieczorek, M., Neumann, G. A., Nimmo, F., Kiefer, W. S., Taylor, G. J., Melosh, H. J., et al. (2013). The crust of the Moon as seen by GRAIL. *Science*, 339(6120), 671–675. <https://doi.org/10.1126/science.1231530>

References From the Supporting Information

Pinel, V., & Jaupart, C. (2000). The effect of edifice load on magma ascent beneath a volcano. *Philosophical Transactions of the Royal Society of London*, 358(1770), 1515–1532. <https://doi.org/10.1098/rsta.2000.0601>